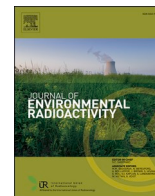


Contents lists available at [ScienceDirect](https://www.sciencedirect.com)

Journal of Environmental Radioactivity

journal homepage: www.elsevier.com/locate/jenvrad

A modeling study on the oceanic dispersion and sedimentation of radionuclides off the coast of Fukushima

Yuki Kamidaira^{a,*}, Yusuke Uchiyama^b, Hideyuki Kawamura^a, Takuya Kobayashi^a, Shigeyoshi Otsaka^c

^a Nuclear Science and Engineering Center, Japan Atomic Energy Agency, Tokai, Ibaraki, Japan

^b Department of Civil Engineering, Kobe University, Kobe, Hyogo, Japan

^c Atmosphere and Ocean Research Institute, The University of Tokyo, Kashiwa, Chiba, Japan

ARTICLE INFO

Keywords:

Fukushima Daiichi nuclear power plant accident
Radiocesium
Suspended radionuclides
Sediment transport
ROMS

ABSTRACT

We developed a three-dimensional prognostic oceanic dispersion model that accounted for the phase transfer of radionuclides between seawater, suspended particles, and seabed sediments with multiscale grain sizes. A detailed hindcast of ¹³⁷Cs in the seabed sediment off the Fukushima coast was conducted to investigate the transfer mechanism of dissolved ¹³⁷Cs derived from the Fukushima Daiichi Nuclear Power Plant (FNPP1) accident toward the seabed sediment. Extensive model-data comparison demonstrated that the model could satisfactorily reproduce the oceanic structure and ¹³⁷Cs concentrations in the seawater and seabed sediment. The model successfully reproduced the major features of the observed spatial variation of the ¹³⁷Cs activities in the sediment, which represented more than 90% of the sedimentary radiocesium existing in the coastal area off Fukushima several months after the accident. Shear stress associated with the resuspension of the seabed sediment was induced by waves near the shore and by current velocity offshore of the study area. The adsorption of ¹³⁷Cs on the seabed sediment differed depending on the particle size, with adsorption on clay being the most substantial. The distribution of ¹³⁷Cs in the sediment off the Fukushima coast was formed mainly owing to adsorption from the dissolved phase by June 2011, when the impact of the direct oceanic ¹³⁷Cs release from FNPP1 was remarkable. After June 2011, seabed sediment became a source of ¹³⁷Cs released to the seawater owing to resuspension with and desorption from the sediment.

1. Introduction

The Great East Japan Earthquake occurred on March 11, 2011, generating catastrophic tsunamis that struck the Tohoku coast. Consequently, substantial amounts of radioactive substances, especially radiocesium (¹³⁴Cs (half-life 2.06 years) and ¹³⁷Cs (half-life 30.2 years)), were released accidentally from the Fukushima Daiichi Nuclear Power Plant (FNPP1) to Pacific coastal waters. After the FNPP1 accident, several observational and computational studies on oceanic radionuclide dispersion and transport have been conducted (e.g., Masumoto et al., 2012; Tsubono et al., 2016). Several years after the accident, the dissolved ¹³⁷Cs concentrations in the coastal shelf water off Fukushima were found to have decreased by dispersal and dilution via the synoptic-scale Kuroshio-Oyashio current system to preaccident background values (Kitamura et al., 2014; Takata et al., 2016). However, compared with the concentration of dissolved radiocesium, that in the

seabed sediment has not decreased remarkably (Kusakabe et al., 2013). Although ¹³⁷Cs concentrations in the coastal shelf sediment off Fukushima have decreased gradually (Kusakabe et al., 2017; Otsaka, 2017; Takata et al., 2017; Tateda et al., 2020), the long-retained radiocesium in the seabed sediment may transfer through the benthic food chain (Sohtome et al., 2014; Bezhenar et al., 2016; Tateda et al., 2016; Wang et al., 2016). Another important reason for evaluating the radiocesium in the seabed sediment in the area is that it contributes radiocesium to the seawater off Fukushima. On the basis of the in situ sampled data, Takata et al. (2016) reported that desorption/dissolution from sediment is one of the main sources contributing ¹³⁷Cs to the inventory of radiocesium in the waters off Fukushima. These results suggest that the estimation of the radiocesium retention capacity of the seabed sediment and evaluation of the radiocesium transfer mechanism between the seabed sediment and water are important for marine environmental assessment.

* Corresponding author.

E-mail address: kamidaira.yuki@jaea.go.jp (Y. Kamidaira).

<https://doi.org/10.1016/j.jenvrad.2021.106724>

Received 20 May 2021; Received in revised form 13 August 2021; Accepted 21 August 2021

Available online 3 September 2021

0265-931X/© 2021 Elsevier Ltd. All rights reserved.

The grain size distribution of the seabed sediment and ^{137}Cs activities in the overlying bottom water are vital for representing simulated ^{137}Cs activities in the sediment (Otosaka and Kobayashi, 2013; Kusakabe et al., 2013; Ambe et al., 2014; Black and Buesseler, 2014; Misumi et al., 2014; Fukuda et al., 2018; Tateda et al., 2020). The numerical hindcast by Misumi et al. (2014) could be regarded as one of the most successful modeling studies on ^{137}Cs in the seabed sediment off the Fukushima coast. In their model, ^{137}Cs transfer between bottom water and sediment with grain size distribution occurs via adsorption and desorption. Its results were generally found consistent with in situ ^{137}Cs measurements, temporally and spatially, although they slightly underestimated ^{137}Cs concentration compared with the observation because the model does not consider ^{137}Cs in the suspended particulate form.

Several modeling studies on oceanic radionuclide dispersion suggest that the interactions of nonconservative radionuclides with particulate matter must be considered. For example, Kobayashi et al. (2007) conducted the oceanic dispersion simulation of ^{137}Cs released from the British Nuclear Fuels Ltd. in the Irish Sea using a numerical simulation model system that consisted of an ocean current model and a Lagrangian particle tracking model. Periañez (2008) performed the oceanic dispersion simulation of ^{137}Cs and $^{239,240}\text{Pu}$ in the Alborán Sea, western Mediterranean, using a quasi-three-dimensional numerical model considering sediment transport. Both models consider the exchanges of radionuclides between the dissolved and solid phases (suspended matter particles and seabed sediments). Consequently, their studies successfully reproduced the main characteristics of the radionuclide migration and movement in the study area. Choi et al. (2013) is the only modeling study of ^{137}Cs off the Fukushima coast that considers the interactions of dissolved radionuclides with particulate matter. They investigated the spatiotemporal variation of Fukushima-derived ^{137}Cs in both seawater and sediment several months after the accident using a coupled Lagrangian particle tracking-ocean circulation model that considers the interactions of dissolved radionuclides with particulate matter. Although they did not compare the simulated results with observed data quantitatively, they found that major adsorption on bottom sediments occurred during the first month after the release, and a large quantity of radionuclides settled on the sea floor at one point.

Sediment resuspension is a source of suspended particulate matter in the ocean, and near-bottom orbital motions due to surface waves are an important factor in resuspension. Bottom stress, which determines the sediment resuspension, depends on the combined effect of waves and currents. Blaas et al. (2007) analyzed suspended sediment transport processes in the Santa Monica Bay and San Pedro Bay using a regional sediment transport model considering the wave-enhanced bed boundary layer. They suggested that surface waves are a dominant factor in the resuspension of bed material on the Southern Californian shelves. Sediment resuspension is vital for a good representation of the radionuclides in the ocean because the radionuclides adsorbed on sediment are also released toward the water by resuspension. However, existing modeling studies investigating the spatiotemporal variation of Fukushima-derived radionuclides in the ocean do not consider the effect of waves on the resuspension.

Recently, the impact of the inflow of radioactive materials from rivers to the coastal margin off Fukushima on the marine environment has become significant (Kitamura et al., 2014; Iwasaki et al., 2015; Kakehi et al., 2016; Ikenoue et al., 2020). A portion of the radionuclides released from FNPP1 into the atmosphere has deposited on the land around FNPP1. These radionuclides that have been adsorbed on surface soil particles are being transported to the ocean through the river channel networks. Radionuclides adsorbed on soil particles have a longer-term impact on the marine environment compared with dissolved radionuclides directly released from FNPP1 because the former takes a longer time to be transported to the ocean due to the hydrological process. In addition, these suspended particles introduced from river discharge and resuspended from the seafloor have different radionuclide adsorption/desorption and transport characteristics for

different particle sizes, thus it will be necessary to evaluate the environmental impact of each particle size. Therefore, a model considering radionuclides adsorbed on multi-size class particles should be developed to assess their impact on the environment.

In the present study, we developed an oceanic dispersion model considering the interactions of dissolved radionuclides with suspended particles and seabed sediment with multiscale grain sizes. A numerical experiment of oceanic three-dimensional (3D) dispersal and initial dilution of the ^{137}Cs released from the FNPP1 accident was conducted using the developed model to investigate the transfer mechanism of ^{137}Cs toward the seabed sediment. Our analysis is based on double-nested ocean downscaling 3D circulation modeling using the Regional Oceanic Modeling System (ROMS; Shchepetkin and McWilliams, 2005; 2008) embedded within assimilative oceanic reanalysis, a four-dimensional (4D) variational ocean reanalysis for the Western North Pacific over 30 years (FORA-WNP30; Usui et al., 2017) product with a lateral grid resolution of $1/10^\circ$ and atmospheric forcing from the assimilative grid point value of the global spectral model (GPV-GSM; e.g., Roads, 2004), and mesoscale model (MSM; e.g., Isoguchi et al., 2010) reanalysis products.

The remainder of this paper is organized as follows. The developed model and modeling framework used for the hindcast experiment for a year following the FNPP1 accident are described in Section 2. Section 3 shows the model results and discusses the sedimentary ^{137}Cs distribution mechanisms. Sections 3.1, 3.2, and 3.3 illustrate an extensive comparison between the model results and field observation and satellite altimetry data to validate the model's capability to reproduce the Kuroshio, 3D oceanic structure, and distribution of ^{137}Cs in the marine environment. Section 3.4 considers the time variation and distribution of near-bed ^{137}Cs and sediment to investigate the transfer mechanism of ^{137}Cs toward the seabed sediment. A summary and the conclusions are given in Section 4.

2. Methods

2.1. Model description

In this study, we developed a 3D oceanic dispersion model that considers the interactions of dissolved radionuclides with multiclass suspended particles and seabed sediments using ROMS. This model is based on the nonconservative radionuclide dispersion model presented by Periañez (2008; 2013) and the sediment transport model presented by Blaas et al. (2007).

The suspended particles and radionuclide transport are described by Eulerian advection-diffusion equations, which consider the vertical settling term and fluxes by the erosion from and deposition onto the seabed sediment. Radionuclides are assumed to exist not only as dissolved radionuclides in the water column but also in suspended matter and the seabed sediment. Since radionuclide adsorption onto and desorption from particles depend on the grain size, we assumed that suspended matter and the seabed sediment have a grain size distribution. Details of the model equations are presented in supplementary materials (S1 Model description).

2.1.1. Sediment transport model

The equation for the time evolution of the suspended matter concentration in seawater with each size class j ($j = 1, 2, \dots, N$) is written as follows:

$$\frac{\partial M_j}{\partial t} + \frac{\partial}{\partial x_i} \{ (u_i - \delta_{i,3} w_{s,j}) M_j \} - \frac{\partial}{\partial x_i} \left\{ K_i \frac{\partial M_j}{\partial x_i} \right\} = S_j, \quad (1)$$

where M_j is the suspended matter concentration in size class j (dimension kg m^{-3}); u_i is the velocity component along the x_i direction (m s^{-1}); K_i is the eddy diffusivity ($\text{m}^2 \text{s}^{-1}$); $w_{s,j}$ is the vertical settling velocity (m s^{-1}), which depends on the sediment grain size but is

independent of flow conditions and concentrations; and S_j represents the sources and sinks of suspended matter ($\text{kg m}^{-3} \text{s}^{-1}$). The subscript $i = 1, 2, \text{ and } 3$ denotes the spatial coordinate (with x_3 vertically upward). The repetition of the Index i implies summation, but Eq. (1) is solved separately for each size class j . The vertical particle settling along the x_3 direction is considered with the Kronecker delta ($\delta_{i,3}$; no unit) on the advection term.

2.1.2. Radionuclide transport model

The equation for the time evolution of the radionuclide concentration in the dissolved phase is written as follows:

$$\frac{\partial C_d}{\partial t} + \frac{\partial(u_i C_d)}{\partial x_i} - \frac{\partial}{\partial x_i} \left(K_i \frac{\partial C_d}{\partial x_i} \right) = \sum_{j=1}^N \left(-k_{1,j}^m C_d + k_2 C_{s,j} \right) - \lambda C_d + S_d, \quad (2)$$

where C_d is the radionuclide concentration in the dissolved phase (Bq m^{-3}); $C_{s,j}$ is the radionuclide concentration in the suspended matter in size class j (Bq m^{-3}); $k_{1,j}^m$ and k_2 are kinetic coefficients for adsorption onto and desorption from the suspended matter (s^{-1}), respectively; λ is the decay constant of the radionuclides (s^{-1}); and S_d represents the sources or sinks of dissolved radionuclides ($\text{Bq m}^{-3} \text{s}^{-1}$). The second and third terms on the left side imply the summation of the terms over all the values of the Index i .

The equation for the time evolution of the radionuclide concentration in the suspended matter in each size class j is written as follows:

$$\frac{\partial(C_{s,j})}{\partial t} + \frac{\partial}{\partial x_i} \{ (u_i - \delta_{i,3} w_{s,j}) C_{s,j} \} - \frac{\partial}{\partial x_i} \left\{ K_i \frac{\partial(C_{s,j})}{\partial x_i} \right\} = k_{1,j}^m C_d - k_2 C_{s,j} - \lambda C_{s,j} + S_{s,j}, \quad (3)$$

where $S_{s,j}$ represents the sources and sinks of radionuclides in the suspended matter ($\text{Bq m}^{-3} \text{s}^{-1}$). The index summation is the same as that in Eq. (1).

The seabed sediment is modeled as a two-layer system similar to those of Reed et al. (1999) and Blaas et al. (2007). The two-layer system has an active layer and a substrate. As is the case for the sediment in their studies, we assume that the radionuclides in the active layer interact with both the water column and substrate, whereas the radionuclides in the substrate do not touch the water column; they only interact with the upper active layer according to the sediment erosion and deposition. The radionuclides in the bottom sediment phase are assumed to be not advected horizontally. The equation for the time evolution of the radionuclide concentration in the seabed sediment active layer in each size class j is written as follows:

$$\frac{\partial A_{s,j}}{\partial t} = k_{1,j}^s \frac{(H_s C_d)|_{x_3=-h}}{L \rho_{s,j} (1-p_j) f_j} - k_2 \phi A_{s,j} + \frac{w_{s,j} C_{s,j}|_{x_3=-h} - E_j A_{s,j}}{L \rho_{s,j} (1-p_j) f_j} - \lambda_{1,j} A_{b,j} - \lambda_{2,j} A_{s,j} - \lambda A_{s,j}, \quad (4)$$

where the first and second terms at the right-hand side represent the interaction between the sediment and the dissolved phase, whereas the third term at the right-hand side represent the interaction between the sediment and the suspended phase; $k_{1,j}^s$ is the kinetic coefficient for adsorption onto the seabed sediment (s^{-1}); ϕ is a correction factor (no unit); $A_{b,j}$ is the radionuclide concentration in the seabed sediment substrate (Bq kg^{-1}); $\lambda_{1,j}$ and $\lambda_{2,j}$ are the kinetic coefficients (s^{-1}) for the adsorption and desorption between the active layer and the substrate, respectively; these coefficients depend on the net flux into the seabed sediment from the water (viz., erosion and deposition of the sediment).

The equation for the time evolution of the radionuclide concentration in the seabed sediment substrate in each size class j is written as follows:

$$\frac{\partial A_{b,j}}{\partial t} = - \frac{L f_j}{L_b f_{b,j}} \left(- \lambda_{1,j} A_{b,j} - \lambda_{2,j} A_{s,j} \right) - \lambda A_{b,j}, \quad (5)$$

where L_b is the thickness of the seabed sediment substrate (m). A

schematic illustration of the interaction processes between the radionuclide phases in the model is presented in Fig. 1.

2.2. Model configuration

We used the state-of-the-art oceanic circulation model ROMS to simulate the circulation off the northeastern Pacific coast of Japan on a double-nested configuration. ROMS is a free-surface, terrain-following, primitive-equation 3D regional hydrodynamic model with a hydrostatic assumption and Boussinesq approximation. We conducted a simultaneous simulation of hydrodynamics and tracer (viz., ^{137}Cs and sediment particles) transport. Fig. 2 shows the numerical domains of the oceanic downscaling model in a double-nested configuration embedded in the FORA-WNP30 domain (not shown). Details of the configurations of hydrodynamic model are presented in supplementary materials (S2 Configurations of hydrodynamic model).

The dispersion model described in Section 2.1 was applied to the ^{137}Cs derived from FNPP1 and the sediment released from the major rivers in Japan and resuspended from the seafloor. The parameters for the sediment and ^{137}Cs are summarized in Tables 1 and 2. The active layer thickness L was assumed to be at least a few median grain diameters thick to centimeter order in previous studies on radionuclide dispersion or sediment transport models (e.g., Blaas et al., 2007; Kobayashi et al., 2007; Periañez, 2013). Kobayashi et al. (2007) and Periañez (2013) set the active layer thickness as $L = 10$ cm and successfully reproduced the main characteristics of radionuclide migration and movement in the ocean. In some observations, significant concentrations of ^{134}Cs were detected even at 10-cm sedimentary layers, especially in coastal regions (e.g., Otosaka and Kato, 2014). In this study, we assumed the thickness of the active layer $L = 10$ cm and horizontally uniform. The remaining parameters for the sediments used in Eqs. (1)–(5) were determined experimentally and consistent with those of Blaas et al. (2007) and Wang (2002), whereas the radionuclide parameters were consistent with those of Periañez (2013).

The ^{137}Cs input into the ocean—that from atmospheric deposition and that directly released from FNPP1—was imposed as dissolved form in the model, as in Kamidaira et al. (2018). The dissolved ^{137}Cs point source was introduced as directly released from FNPP1 into the ocean on the basis of in situ ^{137}Cs measurement (Kawamura et al., 2011). The ^{137}Cs point source was imposed in the grid adjacent to FNPP1 from March 26, 2011 to June 30, 2011. The release rate reached 1.67×10^{-2} PBq h^{-1} on April 10, started to decrease, and reached the order of 10^{-4} PBq h^{-1} by the end of April.

We also adopted data on the atmospheric deposition at the sea surface as the area source of dissolved ^{137}Cs ; the data were from the Worldwide version of System for Prediction of Environmental

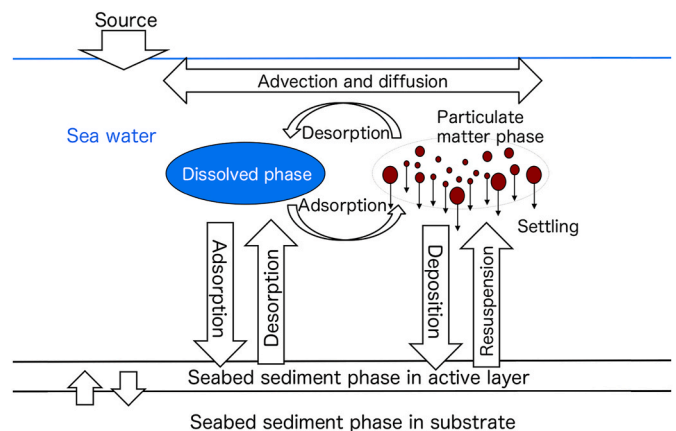


Fig. 1. Schematic of the interaction processes between the radionuclide phases in the model.

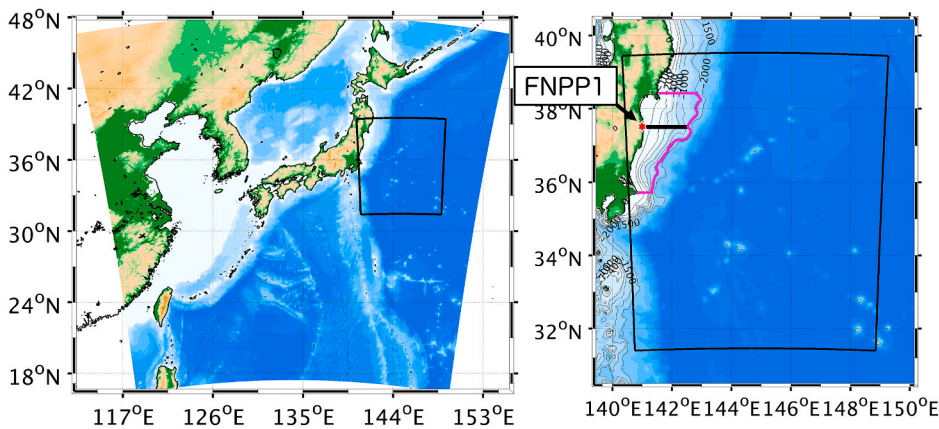


Fig. 2. Double-nested ROMS model domains for the parent ROMS-L1 (left plot) and its enlarged view (right)—the child ROMS-L2 model domain is illustrated using black solid boxes in both panels; bathymetry down to the depth of 2000 m is shown using black contours (m); the red star indicates the location of Fukushima Daiichi Nuclear Power Plant (FNPP1); the thick black line identifies the transect for the cross-sectional plots in Figs. 13 and 14; and the inventory of sedimentary radiocesium in Fig. 12 was estimated for the area inside the magenta line. (For interpretation of the references to color in this figure legend, the reader is referred to the Web version of this article.)

Table 1

Parameters for each grain size using in sediment transport model. d_j : the diameter of the particles, $\rho_{s,j}$: the particle dry weight density, $w_{s,j}$: the vertical settling velocity, $E_{u,j}$: the entrainment rate, $\tau_{cr,j}$: the critical bed shear stress.

Class name	d_j (μm)	$\rho_{s,j}$ (kg m^{-3})	$w_{s,j}$ (mm s^{-1})	$E_{u,j}$ (kg m^{-2} s)	$\tau_{cr,j}$ (N m^{-2})
Sand	125	2650	9.4	2.5×10^{-3}	0.15
Silt	24	2650	0.4	1.0×10^{-4}	0.07
Clay	4	2650	0.1	1.0×10^{-4}	0.02

Table 2

Sediment and ^{137}Cs parameters using in sediment and radionuclide transport model.

Parameter description	Value
Thickness of the active layer	$L = 10$ cm
Initial thickness of the substrate	$L_b = 1$ m
Porosity	$p = 0.4$
Kinetic coefficient for desorption from suspended matter	$k_2 = 1.16 \times 10^{-5}$ s^{-1}
Correction factor	$\phi = 0.01$
Exchange velocity	$\chi = 2.1 \times 10^{-8}$ ms^{-1}

Emergency Dose Information version II (WSPEEDI-II; Terada and Chino, 2008). The ^{137}Cs release amount from March 12, 2011 to April 30, 2011 estimated by Katata et al. (2015) was applied as the atmospheric release rate for WSPEEDI-II. The WSPEEDI-II model domain encompasses the ROMS-L1 domain, with a horizontal resolution of 10 km in both the latitudinal and longitudinal directions. The three-hourly deposition amount of the airborne radioactive ^{137}Cs predicted by WSPEEDI-II was assumed to have deposited in the dissolved form at the sea surface from March 12, 2011 to May 31, 2011.

On the other hand, the ^{137}Cs input from rivers were not considered. Based on the Universal Soil Loss Equation (USLE), Kitamura et al. (2014) estimated annual amount of ^{137}Cs discharge to the ocean from the 14 river basins in 2011 within the ROMS-L2 domain to be 8.4TBq, whereas the amount of direct oceanic discharge from FNPP1 was about 3.5PBq. Therefore, the influence of ^{137}Cs input from rivers during the analysis period is considered to be small.

The ^{137}Cs released into the ocean as particulate matter was not considered ($S_{s,j} = 0$; $F_{s,j}^{\text{atm}} = 0$) because its quantity was considerably smaller than that of the dissolved ^{137}Cs released from FNPP1 within the study period. In this study, we only considered the ^{137}Cs derived from FNPP1 to understand its dynamics in the ocean, although ^{137}Cs had been existing in the marine environment due to a global fallout before the accident ($1\text{--}2$ Bq m^{-3} in seawater; $1\text{--}2$ Bq kg^{-1} in seabed sediment; e.g., Kusakabe et al., 2013). Thus, the initial conditions of ^{137}Cs in all phases of the ROMS-L1 and ROMS-L2 models were set to zero.

The suspended matter in this study was considered to be the land-derived sediment particles introduced from river discharge and resuspended from the seafloor. We took into account three size classes: sand ($d_1 = 125$ μm), silt ($d_2 = 24$ μm), and clay ($d_3 = 4$ μm). We assumed that all sediment fractions were non-cohesive. The initial distribution of the sediment bed composition of the ROMS-L1 model was obtained from the spatiotemporally interpolated fraction fields of dbSEABED (Jenkins, 1997, 2002), which is a database based on laboratory measurements and descriptive observations. Fig. 3 shows the initial condition of the sediment fractions imposed on the ROMS-L2 domain. Sand is mainly distributed in the coastal region, whereas the other fine sediments are distributed offshore.

The suspended matter flux from atmospheric deposition was not considered in our application ($F_j^{\text{atm}} = 0$). The sediment volume fluxes from rivers have a strong correlation with river discharge (e.g., Taniguchi et al., 2019). Uchiyama et al. (2014) estimated the average cross-sectional concentration at the mouth of a river using an equation that relates the river discharge to the river basin area. This equation is based on the empirical L-Q (discharge to sediment flux) relation proposed by Takekawa and Nihei (2013). The cross-sectional averaged sediment concentration (\bar{c} ; mg l^{-1}) is obtained as follows:

$$\bar{c} = a \frac{Q^{b-1}}{A^{b-1}}, \quad (6)$$

where Q is the river flow flux ($\text{m}^3 \text{s}^{-1}$); A is the river basin area (km^2); and a and b are constant coefficients ($a = 160.0$, $b = 1.62$). Q and A are estimated from the monthly climatology data of the major river discharges compiled by the Japan River Association. The fractions of the three sediment classes in the riverine discharge are determined empirically on the basis of the outcome of the USLE-based river sediment modeling conducted by the JAEA. The sediment flux ratio is assumed to be 5:4:2 (sand:silt:clay) uniformly for all Japan rivers in reference to the river simulation result obtained using the USLE-based model in Yamaguchi et al. (2014).

We conducted a simultaneous simulation of the hydrodynamics and tracers in the ROMS-L1 and ROMS-L2 models. The tracer simulation results from the ROMS-L1 model were set as the boundary and initial conditions for the innermost ROMS-L2 model. In this manner, the effect of the ^{137}Cs deposited outside the ROMS-L2 region and re-influx of tracers discharged outside the ROMS-L2 region were regarded as the boundary conditions of ROMS-L2.

3. Results and discussions

3.1. Model validation

We compared the model results with satellite and in situ observations to validate the reproducibility of the hydrodynamics. The activity of

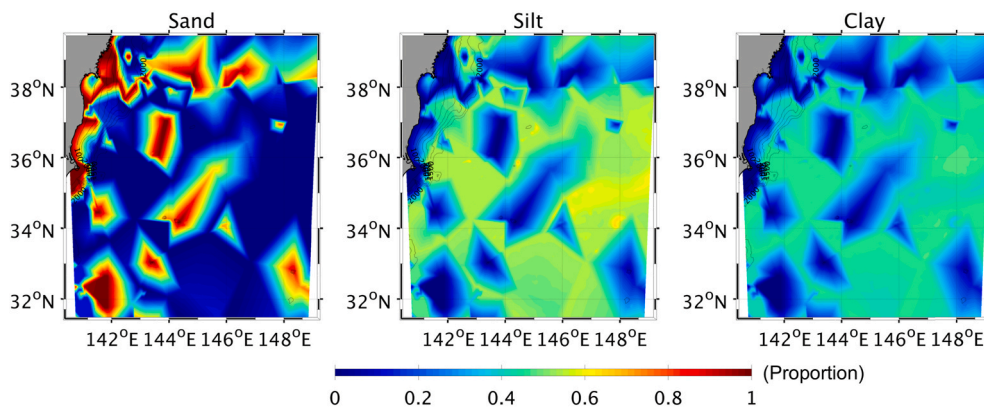


Fig. 3. Initial condition of the sediment proportions with bathymetry down to 2000-m depth in black contours (m).

dissolved ^{137}Cs is crucial for better reproducibility of ^{137}Cs activity in seafloor sediment. Thus, we verified the modeled dissolved ^{137}Cs concentrations, in addition to the oceanic flow field, against data observed from in situ water sampling.

Fig. 4 shows a comparison between the surface velocity (horizontal velocity of the topmost grid cells) magnitude from the ROMS-L2 model results and that from the Aviso delayed-time mapped absolute dynamic topography from multiple satellite altimetry data (gridded daily composite at $1/4^\circ$ resolution; e.g., Le Traon et al., 1998). Overall, the model results agreed with the Aviso data in terms of both magnitude and spatial patterns, including the Kuroshio meandering through March–June 2011, which have a significant effect on the initial dilution of the dissolved ^{137}Cs . For instance, both the model results and the satellite altimetry data showed the existence of a mesoscale eddy at around 39°N and the Kuroshio meandering at around 144°E , confirming the reproducibility of mesoscale variability.

Fig. 5a shows a scatter diagram of the modeled and measured near-bed temperatures in the coastal areas off Fukushima. The observed data are based on CTD measurements from vessels at sampling stations (Oikawa et al., 2013), as shown by the circles in Fig. 7. The temperature of the bottom-most grid cells from ROMS-L2 agreed well with the observational data, with a correlation coefficient R of 0.9485, root mean

square error (RMSE) of 1.432, and model skill score of 0.9735 (a model skill score of one indicates perfect agreement, and zero means complete disagreement; Wilmott, 1981). These results suggest that ROMS-L2 had satisfactory reproducibility in terms of synoptic dynamics, including the Kuroshio path and the oceanic flow field near FNPP1.

Observations by the Ka'imikai-o-Kanaloa (KOK) cruise were regarded as an offshore ^{137}Cs dataset for June 2011 (Buesseler et al., 2012) for the 3D spatial distribution. The modeled dissolved ^{137}Cs activity in the surface water (topmost grid cells) was compared with the activity measured on June 06–18, 2011 by the KOK cruise; these activities are superposed as colored circles in Fig. 6. Overall, the ROMS-L2 model reproduced the observations reasonably well, presenting high concentrations near the shore and decreasing trends in the Kuroshio downstream region. A scatter diagram of the modeled versus measured dissolved ^{137}Cs is shown in Fig. 5b (the available observational data of Buesseler et al. (2012) from the surface to 1000-m depth were used). The reproducibility of radionuclide concentration by the oceanic dispersion model is evaluated by an index, factor 10, which is the ratio of the modeled values to the observed values by a factor of $1/10$ to 10 (e.g., Kamidaira et al., 2018). A large proportion of the modeled ^{137}Cs was within the range of a factor 10, as indicated by the dotted lines, relative to the measured ^{137}Cs with 81.8%, with an apparent improvement

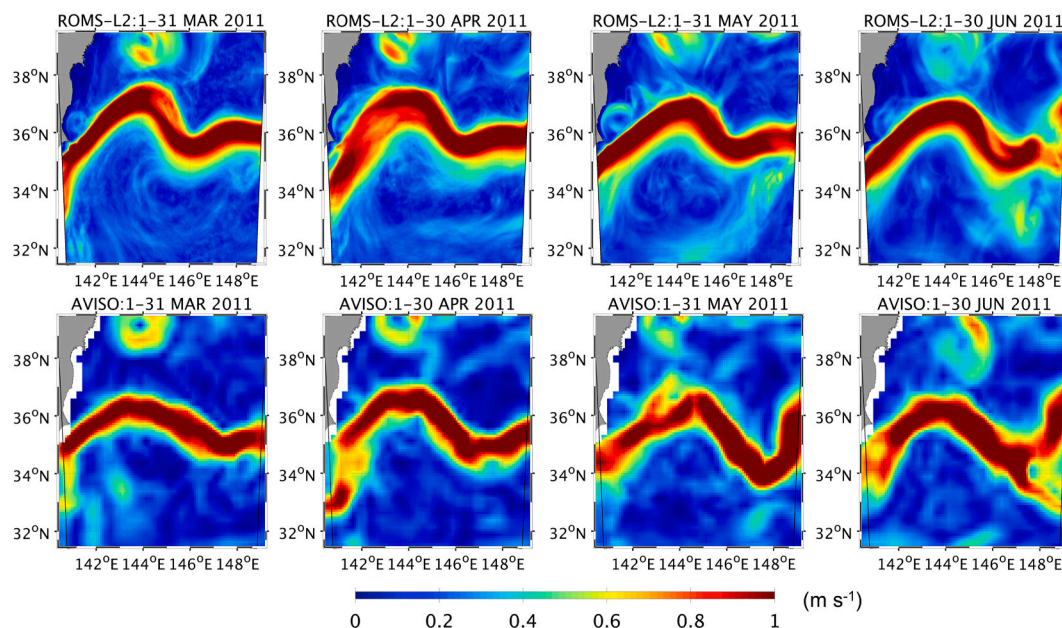


Fig. 4. Plan view plots of time-averaged surface velocity magnitude—the upper plots are the ROMS-L2 result, whereas the lower plots are based on Aviso satellite altimetry.

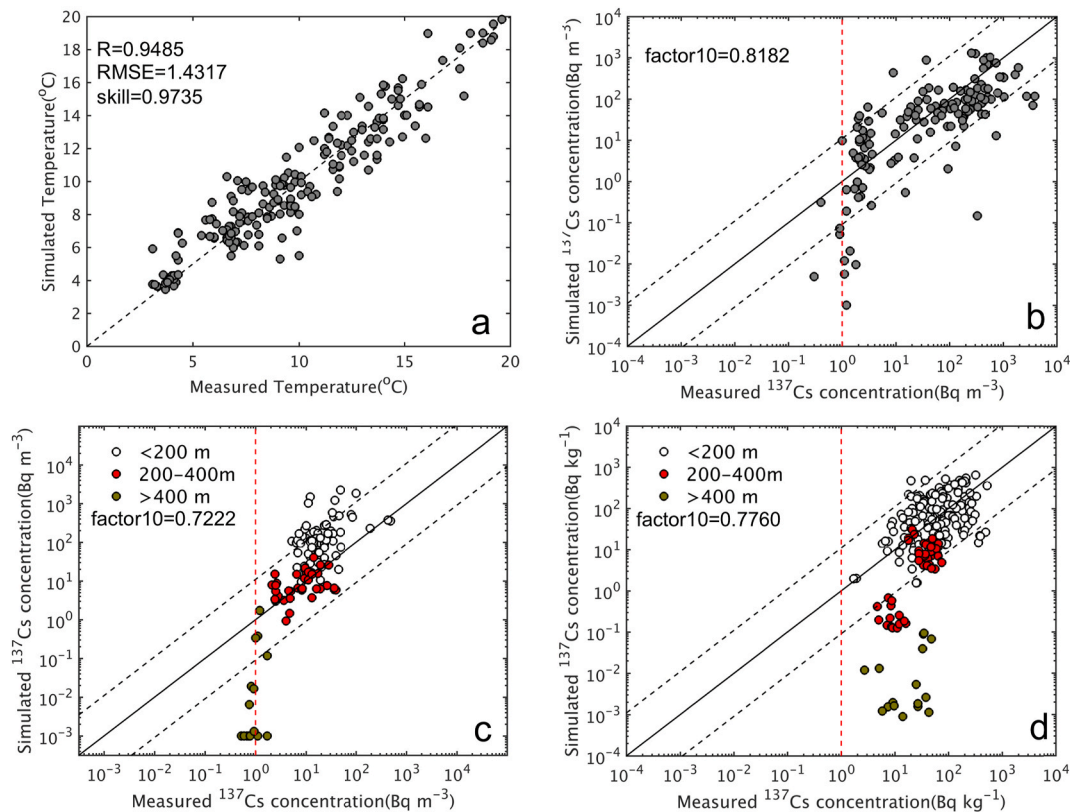


Fig. 5. Scatter diagrams of the various quantities from the ROMS-L2 results—(a) temperature against the in-situ sampled data (Oikawa et al., 2013); (b) dissolved ^{137}Cs concentrations against the in-situ sampled data (Buessler et al., 2012); (c) near-bed dissolved ^{137}Cs concentrations against the in-situ sampled data (Oikawa et al., 2013); (d) ^{137}Cs concentrations in the seabed sediment against the in-situ sampled data (Kusakabe et al., 2013); the solid line represents the 1:1 correlation; it is bounded using two dashed lines indicating deviations with the factors of 1/10 and 10 in Fig. 5b–d; and the white, red, and brown circles are the data from stations at the water depths of <200, 200–400, and >400 m, respectively. The red dotted lines are the orders of magnitude of preaccident background values of the ^{137}Cs concentrations. The in-situ data of Fig. 5a, c, and d are measured in May, June, July, September, October, December 2011, and February 2012. The in-situ data of Fig. 5b are measured in June 2011. R, correlation coefficient, RMSE, root mean square error, and skill, model skill score. (For interpretation of the references to color in this figure legend, the reader is referred to the Web version of this article.)

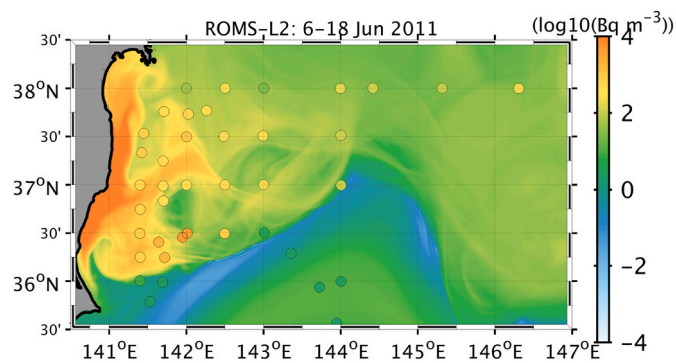


Fig. 6. Modeled dissolved ^{137}Cs concentrations (indicated by colors) from ROMS-L2 at the surface—the colored circles (using the same color scale) indicate the instantaneous in-situ concentrations measured in June 2011 (Buessler et al., 2012). (For interpretation of the references to color in this figure legend, the reader is referred to the Web version of this article.)

compared with the result of Kamidaira et al. (2018), whose regional model underestimated the measured ^{137}Cs considerably at the horizontal resolution of 1 km. They did not consider the inflow of ^{137}Cs from outside the model domain as a boundary condition of their innermost model. This result suggests that the parent model results should be taken into account as recurring influxes through boundaries to enhance reproductivity in terms of the regional modeling of the dissolved ^{137}Cs

concentration derived from FNPP1. This is consistent with the proposal of Tsumune et al. (2013), who also considered the inflow of ^{137}Cs outside the model domain into the regional model.

Oikawa et al. (2013) observed dissolved ^{137}Cs activities at the same monitoring stations as those of the temperatures in Fig. 5a. The modeled near-bed dissolved ^{137}Cs activity concentrations (*i.e.*, concentrations of the bottom-most grid cells) were compared with those measured by Oikawa et al. (2013), and the two sets of findings are superposed as colored circles in Fig. 7. The ROMS-L2 model exhibited a high concentration in Sendai Bay, Japan (around 38°N), in May and a southward along-shelf transport of ^{137}Cs after June. Overall, the concentrations of ROMS-L2 were comparable with the observations; high concentrations appeared in shallow near-shore areas. A scatter diagram of the modeled versus measured near-bed dissolved ^{137}Cs is shown in Fig. 5c. A large proportion of the modeled ^{137}Cs was within an order of magnitude of the measured ^{137}Cs , with a factor 10 of 72.2%, but it was slightly overestimated at the stations shallower than 200 m and underestimated at the stations deeper than 400 m. The modeled dissolved ^{137}Cs dispersal in the coastal area, which occurred several months after the accident, is shown in Fig. 8. Until the middle of March, dissolved ^{137}Cs from atmospheric deposition contaminated shallow coastal areas and reached depths reaching 100 m. Afterward, the direct release of dissolved ^{137}Cs from FNPP1 started, and ^{137}Cs was transported to Sendai Bay. The concentration in Sendai Bay was high until the end of May. Then, the radionuclides were transported southward along the shelf due to a reduction in the mesoscale eddy (centered at 36.5°N , 141.4°E) associated with an approaching tropical cyclone. On the basis of an

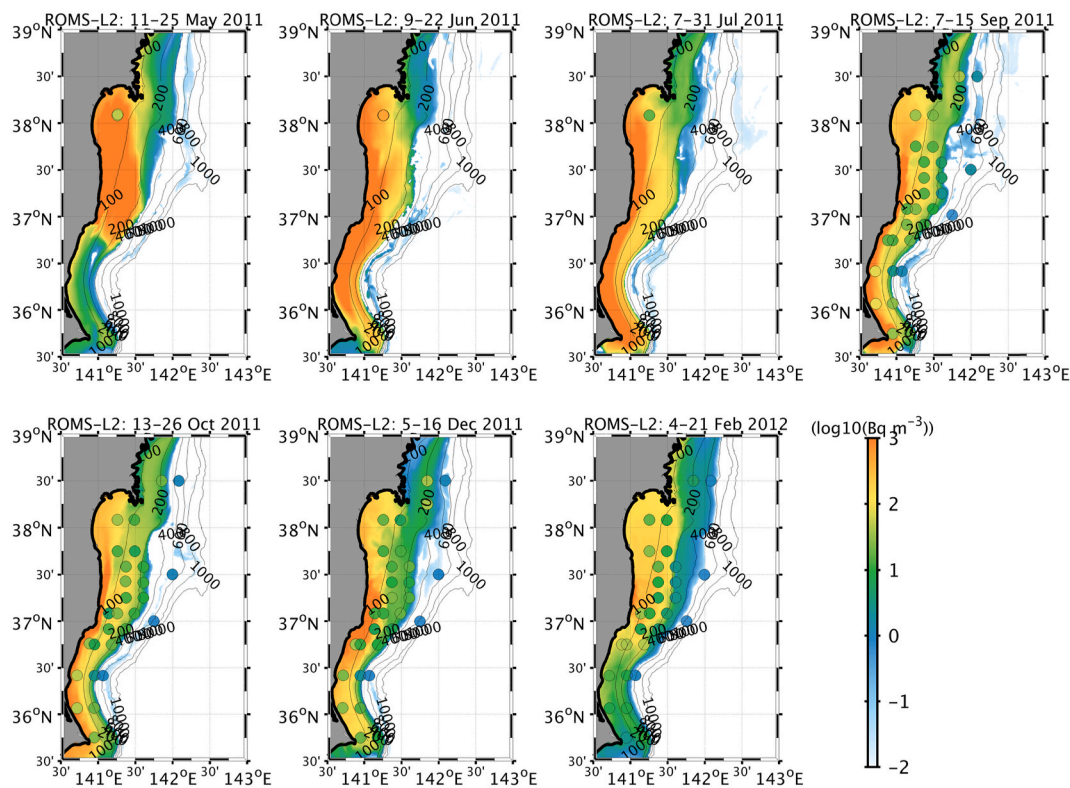


Fig. 7. Modeled near-bed dissolved ^{137}Cs concentrations (indicated by colors) from ROMS-L2 with bathymetry in black contours (m)—the colored circles (using the same color scale) indicate the instantaneous in-situ concentrations measured in May, June, July, September, October, December 2011, and February 2012 (Oikawa et al., 2013). (For interpretation of the references to color in this figure legend, the reader is referred to the Web version of this article.)

observational approach, Aoyama et al. (2012) reported the same ^{137}Cs transport mechanism by the mesoscale eddy. It was considered that the overestimation of the simulated dissolved ^{137}Cs concentration on the coast, despite the overall reproducibility of the flow field, was due to the smoothing of the short time scale coastal flow by TS-nudging. In addition, the observed dissolved ^{137}Cs concentrations at the stations deeper than 400 m were $0.1\text{--}2\text{ Bq m}^{-3}$; these were near the background value, which was not considered in the present study. Thus, ROMS-L2 successfully reproduced the 3D distribution and dynamics of ^{137}Cs derived from FNPP1 along the coast off Fukushima.

In summary, the double-nested ROMS model in this study is satisfactorily capable of reproducing the behavior of the Kuroshio path and 3D oceanic structure in the coastal area off Fukushima, while the modeled dissolved ^{137}Cs reasonably agreed with observations.

3.2. ^{137}Cs in seabed sediment

We verified the modeled ^{137}Cs concentrations in the seabed sediment against observed data obtained from in situ sampling. Kusakabe et al. (2013) investigated ^{137}Cs concentrations in the seabed sediment off the coast of FNPP1 from the same monitoring cruise as that in Oikawa et al. (2013). Fig. 9 shows a comparison between the modeled and observed ^{137}Cs concentrations in the seabed sediment, which are superposed as colored circles. The results from ROMS were the average values for three particle sizes (*i.e.*, sum of the concentrations of the three particle grain sizes per unit weight of the particles). The high ^{137}Cs concentrations in the sediment were distributed along the shore, mainly near FNPP1. Similar to the distribution of the near-bed dissolved ^{137}Cs (Figs. 7), ^{137}Cs concentration increased along the shore from 36°N to 37°N after June. These trends were consistent with the distribution of the observed values.

However, ROMS underestimated the observed values on the shelf slope at depths deeper than 200 m. The scatter plot shows that most of

the simulated concentrations were within one order of magnitude of the observed values, with a factor 10 of 77.60% (Fig. 5d). ROMS reproduced the observations reasonably well, especially at the stations shallower than 200 m, but it tended to underestimate at the stations deeper than 200 m. In particular, ROMS did not reproduce most of the low observed ^{137}Cs concentrations at the stations deeper than 400 m. These low ^{137}Cs activities observed in deeper areas were $2\text{--}60\text{ Bq kg}^{-1}$, which were higher than the preaccident background value, suggesting that they were derived from FNPP1.

As shown in Section 2, ^{137}Cs may have transferred to the seabed sediment from the seawater via adsorption (in the dissolved phase) and deposition (in the suspended phase). Time series of near-bed dissolved ^{137}Cs concentration and ^{137}Cs concentration in the sediment are shown in Fig. S1 (supplementary materials). The simulated ^{137}Cs concentrations in the sediment were comparable to observations at the stations shallower than 200 m despite overestimation of coastal bottom water dissolved concentrations. The numerical hindcast by Misumi et al. (2014), which did not consider the suspended matters, showed the same trend as this study. They suggested that because of the slow adsorption/desorption timescale, the simulated temporal variation of ^{137}Cs in sediments is smoothed relative to that in the overlying bottom water. Although our model takes into account the suspended matters, it can still be regarded as a result of the predominance of adsorption from the dissolved form in the formation of the initial distribution of sedimental ^{137}Cs in the coastal area. On the other hand, ROMS underestimated the observed concentrations of the near-bed dissolved ^{137}Cs at depths greater than 400 m (Figs. 5c and 7, and S1). However, the observed dissolved ^{137}Cs concentrations at depths greater than 400 m were about the same as the preaccident background value; thus, they could not be attributed to the sedimentary ^{137}Cs distribution formation. Therefore, these low ^{137}Cs concentrations in the sediment in the deeper areas may have transferred in the suspended phase.

Otosaka and Kato (2014) showed that the dominant process of

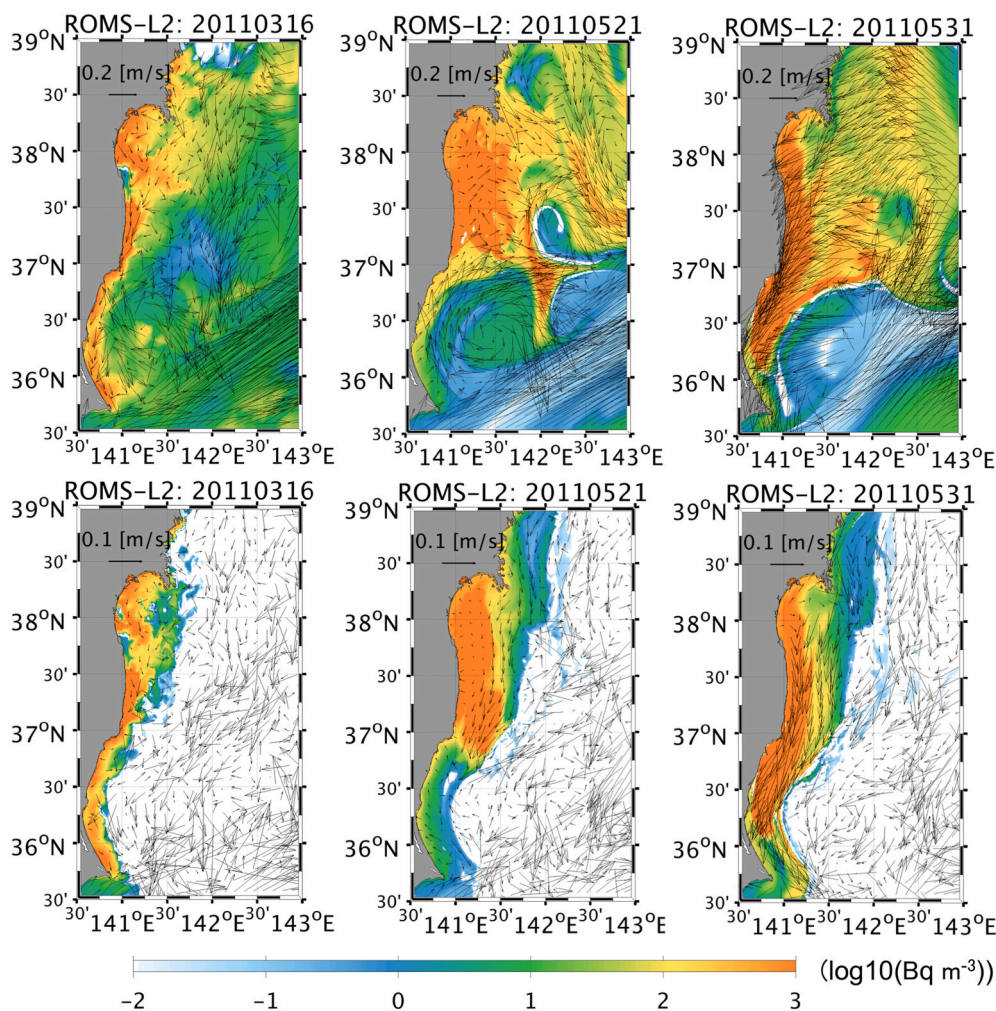


Fig. 8. Daily-averaged spatial distributions of surface dissolved ^{137}Cs concentrations from ROMS-L2 at the surface (upper plots) and of the bottom-most grid cells (lower plots) in March 16, May 21, and May 31, 2011—the black vectors represent the daily-averaged velocity.

incorporating radiocesium into sediments differs at a depth of about 200 m from the relationship between the inventory of radiocesium in sediments and bottom depth. Specifically, it is inferred that dissolved radiocesium in seawater is predominantly adsorbed on sediments in the coastal areas, and scavenging of radiocesium from the surface layer is predominant in the offshore areas. In addition, [Otosaka et al. \(2014\)](#) installed a sediment trap at a station at 873-m depth about 100-km east of FNPP1 over two years after the FNPP1 accident and performed time-series sampling of sinking particles. They observed ^{137}Cs concentrations reaching 400 Bq kg^{-1} in the suspended matter. According to their study, the primary mechanisms for the accumulation of ^{137}Cs in the offshore seabed within five months after the accident were adsorption of ^{137}Cs onto particles (mainly organic or biological) in the surface layer and rapid sinking. They also reported the proportion of these suspended particles that contributed to the formation of the ^{137}Cs distribution in the sediment. About 60% or more of these particles were of biological and organic origin, and rather low lithogenic contents. [Fig. 10](#) shows the ^{137}Cs concentration in the near-bed suspended matter (averaged values for sand, silt, and clay) produced by the model. The distribution pattern was similar to those of the dissolved ^{137}Cs and the ^{137}Cs in the seabed sediment. There was no dominant suspended ^{137}Cs on the shelf slope at depths below 200 m, while the high concentrations observed in [Otosaka et al. \(2014\)](#) were not reproduced by the model.

[Fig. 11](#) shows the simulated near-bed suspended sediment concentration (sum of the weight concentrations per unit volume of the three particle grain sizes). High sediment concentrations were mainly

distributed in the shallow areas 100 m or less; they hardly appeared on the shelf slopes between 100 and 600 m. This was attributed to the distance from rivers, which are less affected by sediment inflow, and weak erosion on the shelf slope. Therefore, suspended sediment was not considered to be involved in the formation of sedimental ^{137}Cs in offshore regions deeper than 400 m. These results suggest that the omission of biological and organic particles from the model may have caused the underestimation of the ^{137}Cs concentration in the deep seabed sediment. Consideration of the process of formation of organic and biological suspended particles at the surface is potentially the key to improving the reproducibility of offshore sedimental ^{137}Cs distributions. For instance, as planktons near the surface of the ocean die and decay, they fall toward the seafloor as particulate matter (called marine snow), adsorbing trace elements and their isotopes (e.g., [Decho and Gutierrez, 2017](#)).

In addition, the thickness of the seabed active layer, where ^{137}Cs adsorbs on and desorbs from the seabed sediment, was assumed to be horizontally uniform in this study. [Otosaka \(2017\)](#) suggested that the active layer thickness off the Fukushima coast has a horizontal distribution; it seems relatively thin (less than 10 cm) in deeper areas. This implies that the proposed model may overestimate the ^{137}Cs desorption from the seabed sediment at deeper depths. Future studies should use a model that includes these biogeochemical processes and considers the horizontal distribution of the active layer thickness.

[Otosaka and Kato \(2014\)](#) estimated the cumulative inventory of radiocesium derived from FNPP1 in the seabed sediment from

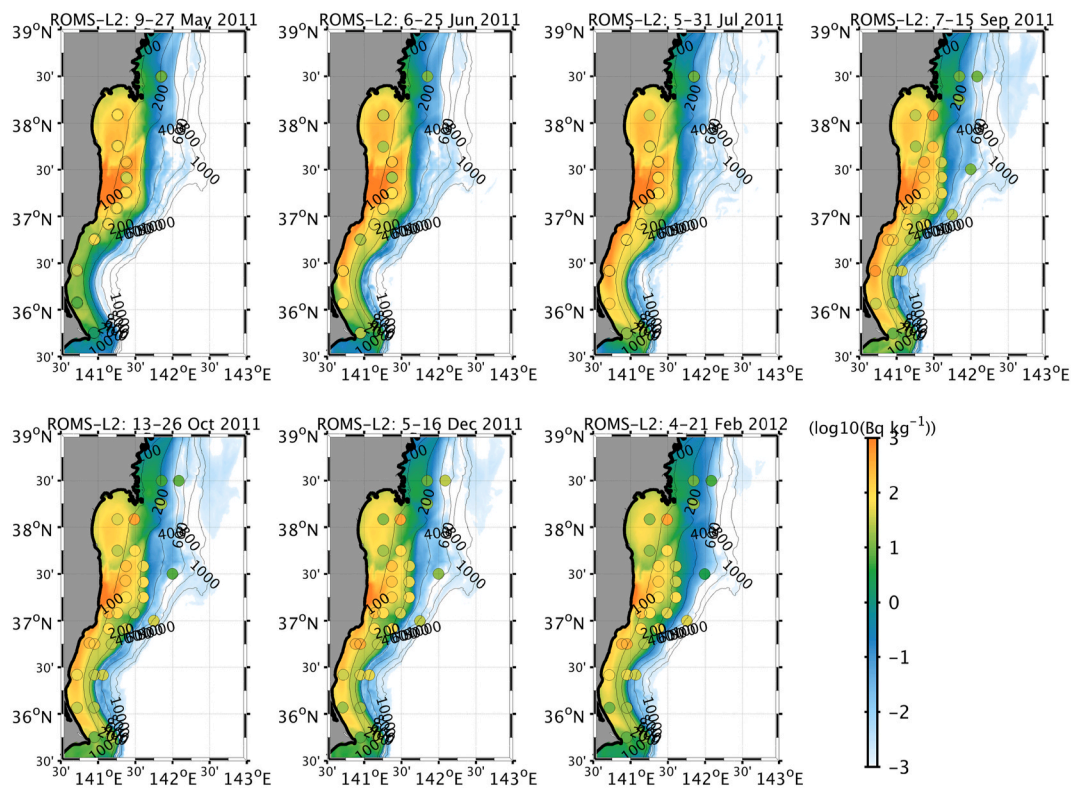


Fig. 9. Modeled ^{137}Cs concentrations in seabed sediment (sum of the concentrations of three particle grain sizes per unit weight of the particles) from ROMS-L2, with bathymetry in black contours (m)—the colored circles indicate the instantaneous in-situ concentrations measured in May, June, July, September, October, December 2011, and February 2012 (Kusakabe et al., 2013).

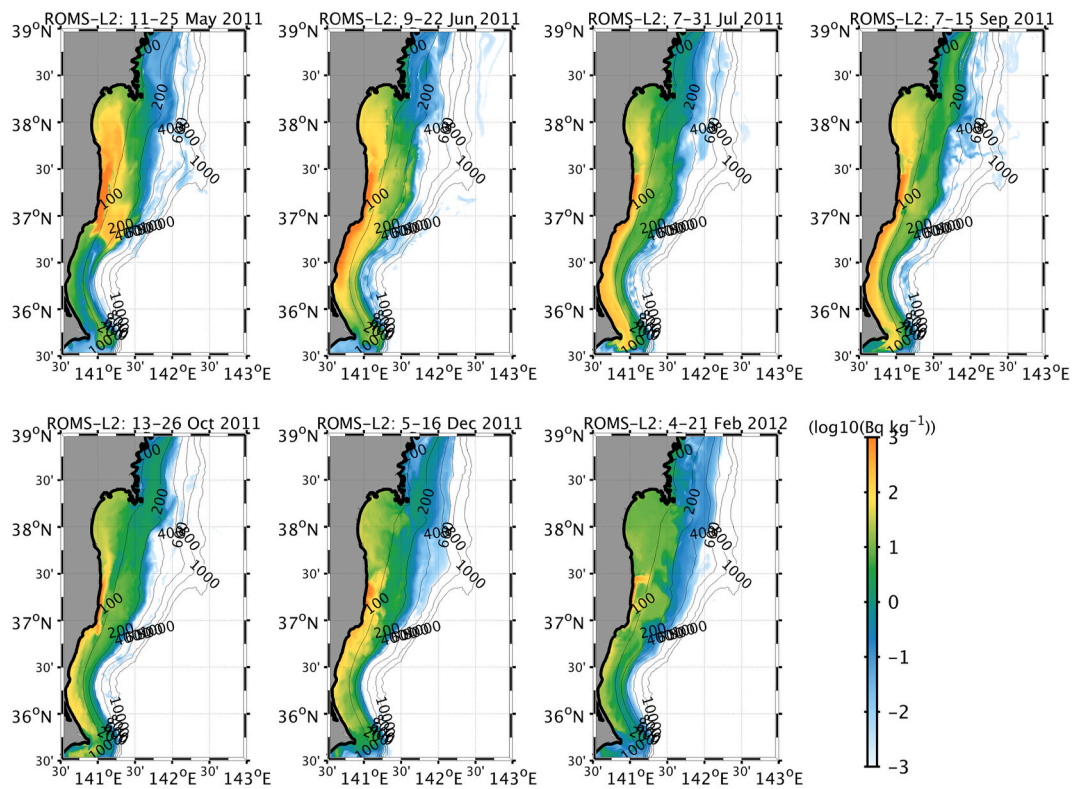


Fig. 10. Modeled near-bed ^{137}Cs concentration in the suspended matter (sum of the concentrations of three particle grain sizes per unit weight of the particles) from ROMS-L2, with bathymetry in black contours (m).

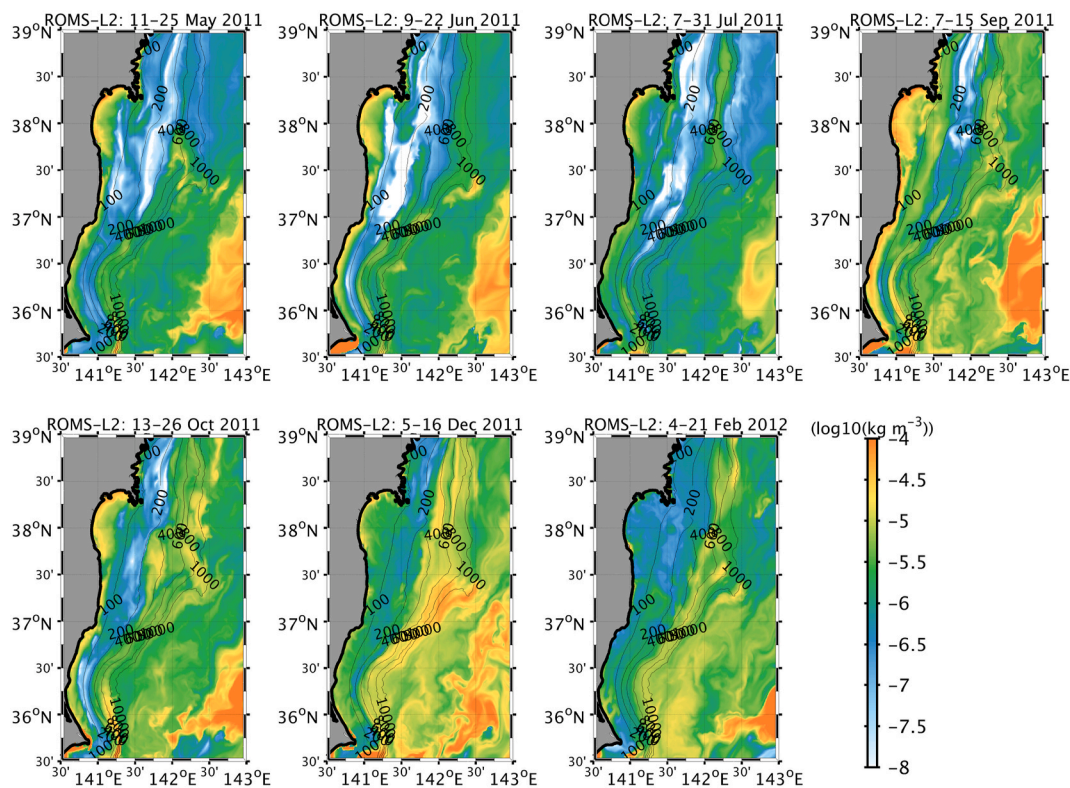


Fig. 11. Modeled suspended sediment concentration (sum of the weight concentration per unit volume of three particle grain sizes) in the bottom water from ROMS-L2, with bathymetry in black contours (m).

observational data in the domain shown in Fig. 2. They estimated the inventory using ^{134}Cs , as ^{137}Cs was released in almost the same amount as that of ^{134}Cs during the FNPP1 accident (e.g., Buesseler et al., 2017). According to their estimate, 200 ± 60 TBq of ^{134}Cs was present in the seabed sediment in the domain in October 2011 (decay corrected to March 11, 2011). The amount of ^{137}Cs in the seabed sediment by our model was estimated to be 450 TBq, which was comparable in orders of magnitude to the observed amount.

Fig. 12a shows the proportion of radiocesium inventory in the sediment, integrated for eight different depth ranges to the total inventory for the depth range of 0–1500 m in October 2011. The inventories from ROMS were calculated in the active layer only (upper 10 cm of seabed sediment). As mentioned earlier, ROMS may have underestimated ^{137}Cs deposition to the seabed sediment via the suspended phase on the offshore shelf slope. Indeed, the inventory at depths below 200 m was less than 1% in the model; the observed inventory was 6.0%. Moreover, most of the modeled radiocesium was in regions shallower than 200 m.

This pattern was consistent with the observations. In the model, 88.8% (10.7%) of the radiocesium was at depths of 0–100 m (100–200 m); the observed estimate was 81.0% (13.0%). Given that the inventory estimations were calculated using 10%–30% of the uncertainty of the observed data, the model inventory can be deemed consistent with the observation. From the above results, we conclude that the sedimentary ^{137}Cs from ROMS overall agreed with the observation, which represents more than 90% of the radiocesium existing in the seabed sediment in the coastal area off Fukushima. On the other hand, the ^{137}Cs distribution on the seabed sediment was underestimated below 400 m mainly due to the omission of biological and organic particles from the model.

3.3. Radiocesium flux from seawater to seabed sediment

In order to evaluate underestimation of sedimentary ^{137}Cs concentration by ROMS-L2 due to the omission of biological and organic particles from the model, we estimated vertical radiocesium flux from

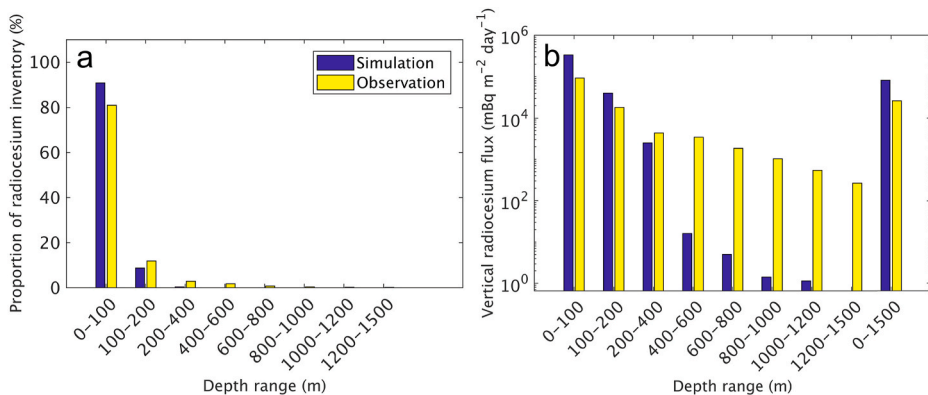


Fig. 12. (a) Proportion of radiocesium inventory in the sediment, integrated for different depth ranges and to the total inventory for depth range of 0–1500 m in October 2011. (b) Area and time averaged vertical radiocesium flux (MF_{Cs}). The inventory and MF_{Cs} were estimated for the area inside the magenta line in Fig. 2. Blue and yellow bars are amount estimated with ^{137}Cs from ROMS-L2, and ^{134}Cs by Otsuka and Kato (2014), respectively. (For interpretation of the references to color in this figure legend, the reader is referred to the Web version of this article.)

seawater to seabed sediment in the domain shown in Fig. 2. Area and time averaged vertical radiocesium flux (MF_{Cs} ; $\text{mBq m}^{-2} \text{day}^{-1}$) is defined by Eq. (7),

$$MF_{Cs} = \frac{Inv_{Cs}}{Area T} \quad (7)$$

where Inv_{Cs} is increase in radiocesium derived from FNPP1 for different depth ranges until October 31, 2011(Bq), $Area$ is area for different depth ranges (m^2), and T is the number of days from March 11, 2011 to October 31, 2011 (234 days). Here, we assumed Inv_{Cs} as inventory in the sediment in October 31, 2011 (^{137}Cs from ROMS-L2 and ^{134}Cs from Ootosaka and Kato, 2014). MF_{Cs} is a quantitative representation of the transfer of dissolved and suspended radiocesium in seawater to seabed sediment.

Fig. 12b show MF_{Cs} for nine different depth ranges for the depth

range of 0–1500 m. The simulated MF_{Cs} showed the same orders of magnitude as observed values in regions shallower than 400 m. Below the 400 m, the simulated MF_{Cs} were two to three orders of magnitude smaller than the observed ones. As discussed in section 3.2, it is considered that the rapid sinking of radiocesium-bound particles at surface observed by Ootosaka et al. (2014) needs to be taken into account in the model to improve the underestimation of offshore MF_{Cs} . According to their results, surface particulate fluxes of ^{137}Cs at 100 km offshore from FNPP1 in March 2011 was in the orders of magnitude of $10^3 \text{ mBq m}^{-2} \text{day}^{-1}$, which decreased exponentially to $10^1 \text{ mBq m}^{-2} \text{day}^{-1}$ in December 2011. On the other hand, simulated MF_{Cs} in the offshore area were in the orders of magnitude of $10^0 \text{ mBq m}^{-2} \text{day}^{-1}$. Thus, scavenging of radiocesium from the surface layer was considered to be mainly due to biological and organic particles. A more sophisticated model that considers biological processes should be developed to

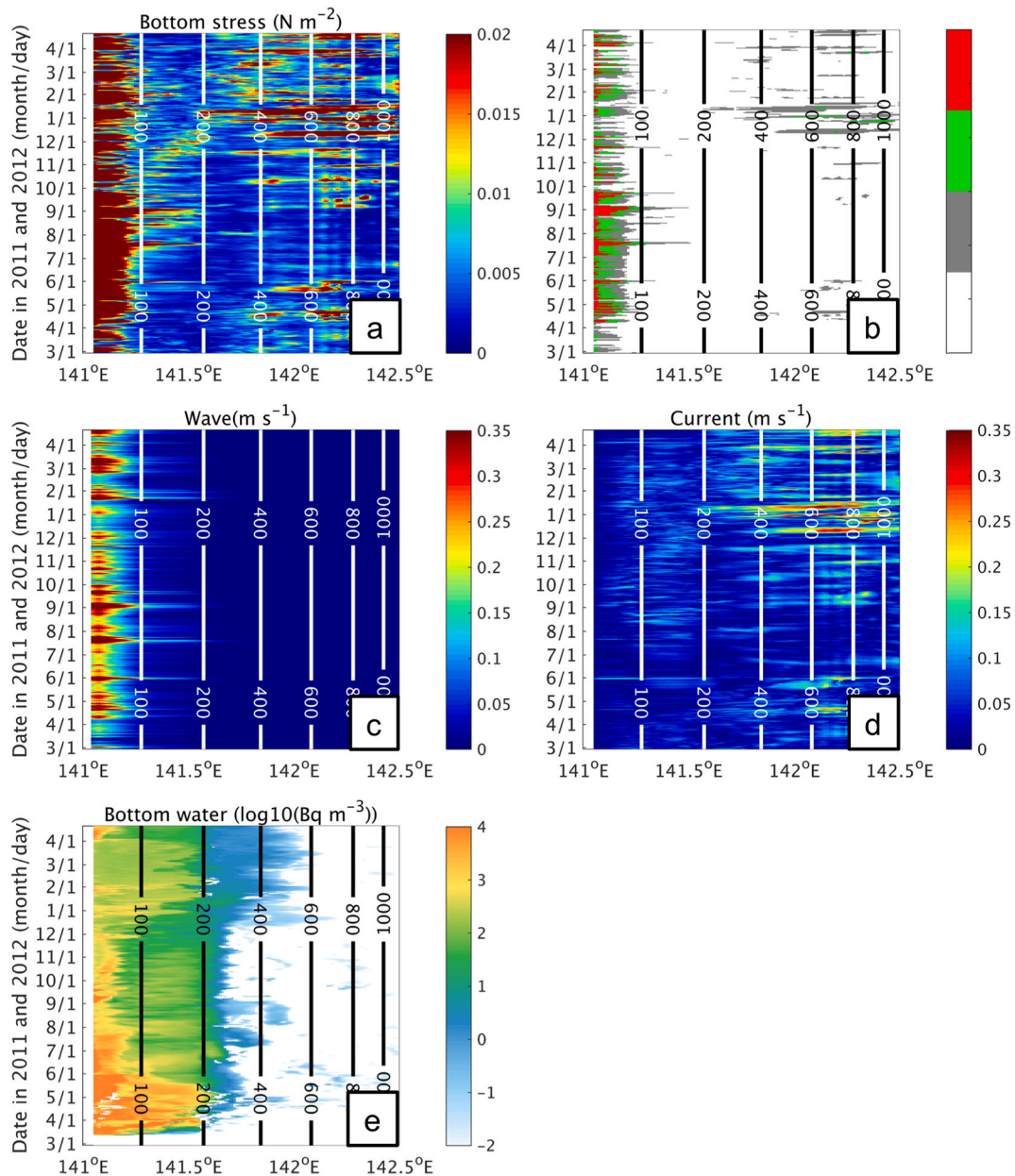


Fig. 13. Hovmöller diagrams across the transect of the various quantities from the ROMS-L2 results, with bathymetry in black and white contours (m)—(a) bottom stress; (b) emerging positions of exceeding the critical bottom stress for sand (red), silt (green), and clay (gray); (c) bottom orbital velocity due to waves; (d) bottom velocity due to mean flow; and (e) near-bed dissolved ^{137}Cs concentration in the bottom water. (For interpretation of the references to color in this figure legend, the reader is referred to the Web version of this article.)

account for the process of ^{137}Cs supply from the surface layer by these sinking particles in the future.

3.4. Time variation and distribution of ^{137}Cs in bottom water and sediment

Hovmöller diagrams of the variables in the bottom-most grid cells and seabed sediment across the transect, as shown by the black line in Fig. 2, are plotted in Figs. 13 and 14 to investigate the transfer mechanism of ^{137}Cs toward the seabed sediment.

Large bottom stresses exceeding the critical shear stress for clay (0.02 N m^{-2} ; Table 1) frequently emerged in coastal regions shallower than 100 m (Fig. 13a). The bottom stresses were weak in the depth range of 100–400 m but occasionally strong in the depth range of 400–1000 m. Fig. 13b shows whether sedimental resuspension occurred. For daily-

averaged bottom stress exceeding the critical bottom stress of any sediment size class, we colored the plot red for sand, green for silt, and gray for clay. Sand was resuspended only in coastal areas shallower than 100 m, while clay and silt could be resuspended even offshore. The bottom orbital velocity due to waves (Fig. 13c) was high only near the shore in coastal regions shallower than 100 m, while the bottom velocity due to mean flow (Fig. 13d) was high mainly in offshore regions deeper than 400 m, with the southward mean flow of the Oyashio current. The strong shear stress distribution near the shore coincides with the area of development of bottom orbital velocity, while strong shear stress distribution offshore coincides with the area of development of bottom current velocity. As mentioned in supplementary materials (S1 Model description), the bottom shear stress was evaluated as a function of the bottom friction of waves (due to the orbital current velocity) and the bottom friction of currents (due to the bottom mean flow), indicating

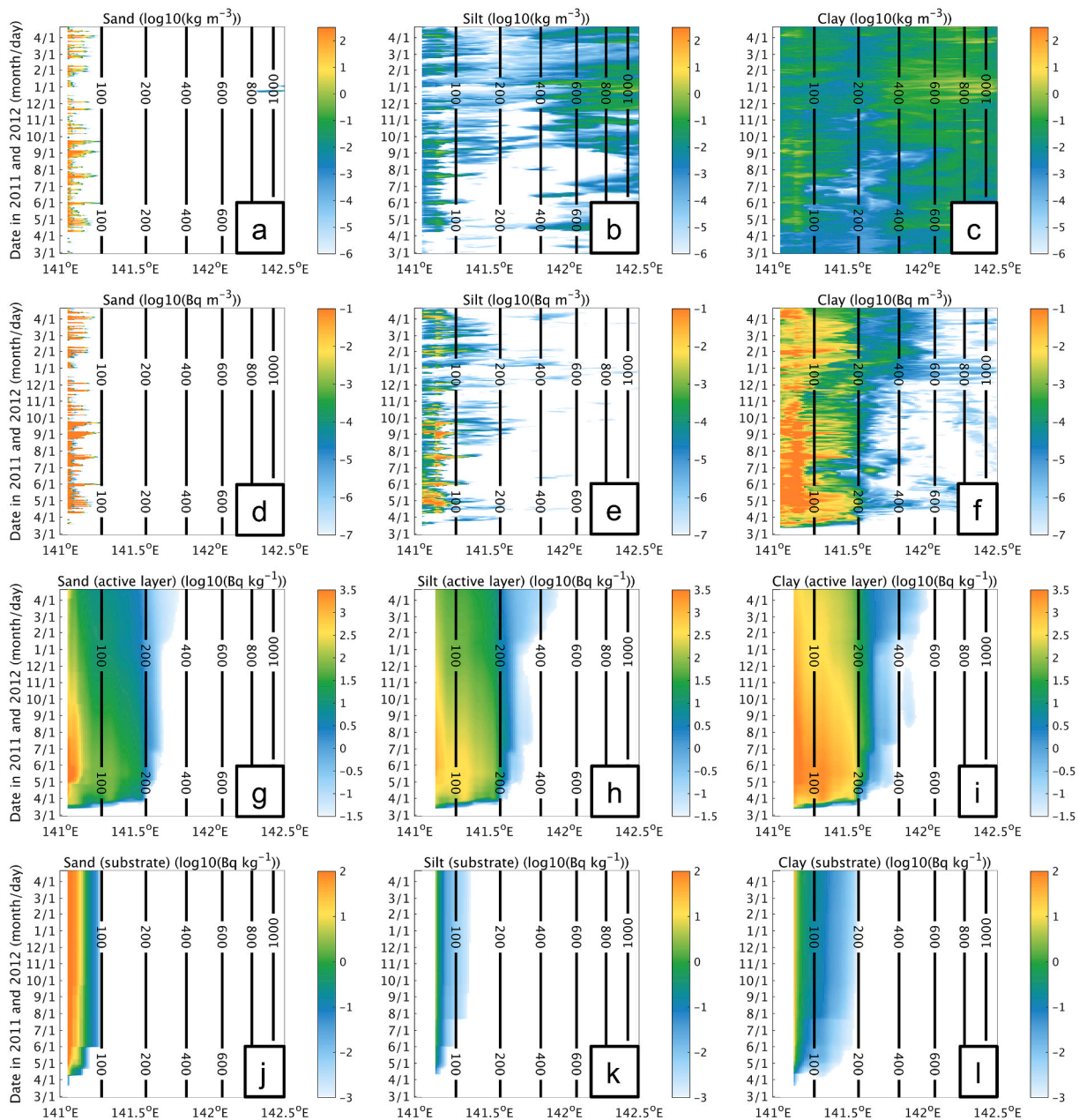


Fig. 14. Same as Fig. 13, but near-bed suspended sediment concentration of (a) sand, (b) silt, and (c) clay; near-bed ^{137}Cs concentration in the suspended matter of (d) sand, (e) silt, and (f) clay; ^{137}Cs concentration in the active layer of the seabed sediment of (g) sand, (h) silt, and (i) clay; and ^{137}Cs concentration in the substrate of the seabed sediment of (j) sand, (k) silt, and (l) clay.

that the shear stress was induced by waves near the shore and by the current velocity offshore on the transect. At depths of 100–400 m on the shelf slope, both orbital and bottom velocities were small, and shear stress did not develop. This condition enabled the fine sediment particles dispersed from the river and shallow water areas to be easily deposited.

The distribution of the near-bed suspended sediments in Fig. 14a–c corresponded to the variation of the bottom stress, indicating that the sediment particles were constantly resuspended in areas with high bottom stress. The distribution of suspended sand grains was limited to shallow coastal areas (100 m or less), which typically have high bottom stresses and large sand fractions (Fig. 3). This finding suggests that sand was transported locally, not horizontally, as vertical transport associated with sedimentation and resuspension. Furthermore, low concentrations of silt and clay were distributed at depths of 100–400 m on the shelf slope offshore, where resuspension barely occurs. We assumed that these fine-grained sediments on the slopes were not produced by local resuspension; instead, they were transported from other sources, e.g., rivers and coastal areas. In regard to the dissolved ^{137}Cs (Fig. 13e), high concentrations reaching depths of 200 m were distributed immediately after the accident until around June 2011, after which they became diluted. Until around June, the influence of ^{137}Cs influx to the ocean through direct release and atmospheric deposition was strong enough to increase the concentration, and the relationship between the concentration fluctuation and bottom stress was unclear. When the ^{137}Cs influx to the ocean from FNPP1 decreased after June, there were increases in dissolved ^{137}Cs concentration associated with strong bottom stresses and a correspondence with fluctuations in suspended ^{137}Cs and sediments (Fig. 14a–f). Since the kinetic coefficient for desorption from suspended matter $k_2 = 1.16 \times 10^{-5} \text{ s}^{-1}$, ^{137}Cs in suspended sediment would desorb into the dissolved form in about one day. Therefore, the concentration fluctuation of the dissolved form after June was considered to be due to ^{137}Cs desorbed from the resuspended sediment into seawater.

The distributions of the near-bed ^{137}Cs in the suspended sediment were limited to the vicinity of the shore for all particle sizes, while they hardly existed offshore despite the resuspension of fine particles (Fig. 13b). The ^{137}Cs attached to clay was the most widespread offshore among all the size classes of particulate grains, but its concentration was several orders of magnitude lower than that of the dissolved phase (Fig. 14f). The distribution of the ^{137}Cs attached to sand was limited near-shore areas shallower than 100 m, but its concentration was high (Fig. 14d). The fluctuation of the ^{137}Cs attached to sand coincided with the appearance of critical shear stress (Fig. 13b), suggesting the dominance of ^{137}Cs transfer to seawater due to resuspension, not desorption from the seabed sand. The concentration of the ^{137}Cs attached to clay increased with resuspension after June. By contrast, it increased with or without resuspension before June, when the influence of ^{137}Cs influx to the ocean from FNPP1 was strong enough to increase the concentration, suggesting that dissolved ^{137}Cs released from FNPP1 was adsorbed on the clay that was advected and dispersed from the rivers and other shallow areas.

Simulated ^{137}Cs in the active sediment layer (Fig. 14g–i) fluctuated less than did the ^{137}Cs in the bottom seawater, i.e., the near-bed dissolved and suspended phases represented in Fig. 13e and Fig. 14d–f, respectively. This suggests that the fluctuation time scale of the ^{137}Cs in the active layer of the sediment was larger than that of seawater advection-diffusion and sediment resuspension. Since the near-bed concentrations of the suspended phases were considerably lower than those of the dissolved phases for all particle grain sizes and varied greatly due to resuspension, adsorption via the dissolved phase was considered the main source of ^{137}Cs in the active layer of the sediment. The patterns of ^{137}Cs distribution in the active layer for each particle grain size were similar, and the difference in concentration between each particle grain size was mainly determined by the difference in the dissolved adsorption kinetic coefficient ($k^s_{1,j}$) for each particle size. The ^{137}Cs in the seabed sediment was mainly distributed in clay and decreased with time while spreading offshore. One year after the

accident, clay at a depth of 400 m had FNPP1-derived ^{137}Cs whose concentrations were at the same level as the preaccident background (Fig. 14i). Significant concentrations were limited to coastal areas shallower than 200 m; the concentrations increased until around June but then started to decrease. This suggests that the sediments acted as a sink of ^{137}Cs until June 2011 and subsequently became a source of the ^{137}Cs released to the seawater after that month via desorption and resuspension with particles.

The concentrations of ^{137}Cs in the sediment substrate increased constantly during the study period for all particle grain sizes (Fig. 14j–l). The largest concentrations were found in sand, but they were limited to coastal areas shallower than 100 m, while small concentrations in clay and silt permeated offshore. As shown in Eq. (5), the concentration of ^{137}Cs in the substrate was determined by sediment deposition and resuspension, which increased with deposition. However, since the difference in ^{137}Cs concentration between the active layer and substrate was several orders of magnitude until at least a year after the accident, the influence of the influx due to deposition to the substrate was more substantial than that of the outflow from the substrate due to resuspension. Thus, the ^{137}Cs concentration in the substrate tended to increase independently by sediment deposition and resuspension. It is expected that ^{137}Cs that has reached deep layers will remain in the sediment for a long time. Since active resuspension occurs along the coast, the ^{137}Cs concentration in the substrate may decrease as the orders of concentration of the active layer and the substrate become more similar.

4. Summary and conclusions

We conducted a detailed hindcast of ^{137}Cs in the seabed sediment off the Fukushima coast using a newly developed model that considers the radionuclide interactions between the dissolved and solid phases with multiscale grain sizes using a double-nested ROMS model embedded within assimilative oceanic reanalysis (FORA-WNP30). We performed extensive model-data comparisons against satellite altimetry data and field observations to demonstrate that the model can satisfactorily reproduce ^{137}Cs concentrations and oceanic structure. The model successfully reproduced the major features of the observed spatial variation of ^{137}Cs activities in the sediment, which represent more than 90% of the radiocesium existing in the coastal area. Hovmöller diagrams across the transect off FNPP1 were used to examine the time variation and distribution of ^{137}Cs in the sediment and the variables that determine the distribution of ^{137}Cs in the sediment.

The results suggested that (1) shear stress was induced by waves near the shore and by current velocity offshore on the transect off the coast of Fukushima; (2) there was the difference in ^{137}Cs adsorption on the sediment per particle grain size, in which adsorption on clay was the most significant; (3) ^{137}Cs permeated into the substrate may be retained in the seabed sediment for a long time; and (4) these ^{137}Cs distributions in the sediment were formed mainly due to adsorption via the dissolved phase by June 2011, when the impact of the direct oceanic release of ^{137}Cs from FNPP1 was significant, while seabed sediment became a source of ^{137}Cs released to the seawater after June 2011, where the ^{137}Cs in the seabed sediment was transferred to the seawater by both resuspension with and desorption from the sediment over a long timescale.

However, the presented model underestimated the ^{137}Cs concentration in the sediment deeper than the depth of 400-m offshore. The low ^{137}Cs distribution observed in the offshore sediment in a previous study suggested a strong involvement of suspended particles of biological and organic origin (Otosaka et al., 2014). Therefore, a more sophisticated model that considers biological processes should be developed in the future.

The parameters for the interactions of ^{137}Cs between the solid phases and sediment movement in this study are the same as those used in previous studies (without any optimization) for the ocean off the coast of Fukushima. Their optimization may improve model accuracy. For

example, the thickness of the active layer in this study was set to be uniform, but observation studies along the Fukushima coast suggest a potential distribution of the ^{137}Cs penetrating the thickness that accords with the topographic slope (Otosaka, 2017; Tsuruta et al., 2017). There is also a lack of literature on radionuclide adsorption/desorption coefficients for the solid phases. Further observations and laboratory experiments are needed to estimate these parameters.

This study showed a small influence of the ^{137}Cs transfer via the suspended phase on the formation of the ^{137}Cs concentration distribution in the sediment off the coast of Fukushima for one year after the accident. However, these effects on the marine environment may have increased several years after the accident. For example, studies indicate that ^{137}Cs deposited on land was released to the ocean in the suspended phase with sedimental matter from rivers several years after the accident (e.g., Kitamura et al., 2014; Iwasaki et al., 2015; Kakehi et al., 2016; Ikenoue et al., 2020). In addition, because of the frequent resuspension of sediment particles along the coast, there is a considerable possibility

that ^{137}Cs with suspended matter will be released to the seawater from the seabed sediment. Thus, researchers should continue to focus on the effects of the seabed sediment on the marine environment as a source of ^{137}Cs released to the seawater. Finally, the proposed radionuclide dispersion model, which accounts for the interaction with solid phases, should be improved and further utilized.

Declaration of competing interest

The authors declare that they have no known competing financial interests or personal relationships that could have appeared to influence the work reported in this paper.

Acknowledgments

This study was conducted using the supercomputer HPE SGI 8600 in the Japan Atomic Energy Agency.

Appendix A. Supplementary data

Supplementary data to this article can be found online at <https://doi.org/10.1016/j.jenvrad.2021.106724>.

Appendix. Table of notations

Notation Definition

$\delta_{i,3}$	Kronecker delta (no unit)
λ	decay constant of the radionuclides (s^{-1})
$\lambda_{1,j}$	kinetic coefficients for the adsorption between the active layer and the substrate (s^{-1})
$\lambda_{2,j}$	kinetic coefficients for the desorption between the active layer and the substrate (s^{-1})
λ_E	straining parameter (no unit)
$\rho_{b,j}$	dry bulk density (kg m^{-3})
$\rho_{s,j}$	particle density (kg m^{-3})
σ_ϕ	standard deviation of the sediment distribution on the sedimentological ϕ -scale
τ_b	magnitude of the shear stress on the grains (N m^{-2})
$\tau_{cr,j}$	critical shear stress for class j (N m^{-2})
ϕ	correction factor (no unit)
χ	exchange velocity (m s^{-1})
A	the river basin area (km^2)
$A_{b,j}$	radionuclide concentration in the seabed sediment substrate (Bq kg^{-1})
$A_{s,j}$	radionuclide concentration in the seabed sediment active layer (Bq kg^{-1})
Area	area for different depth ranges (m^2)
C_d	radionuclide concentration in the dissolved phase (Bq m^{-3})
$C_{s,j}$	radionuclide concentration in the suspended matter in size class j (Bq m^{-3})
D_j	deposition flux onto the seabed sediment active layer ($\text{kg m}^{-2} \text{s}^{-1}$)
$E_{0,j}$	empirical entrainment rate ($\text{kg m}^{-2} \text{s}^{-1}$)
E_j	erosion flux from the seabed sediment active layer ($\text{kg m}^{-2} \text{s}^{-1}$)
F_d^{am}	dissolved radionuclide flux from atmospheric deposition ($\text{Bq m}^{-2} \text{s}^{-1}$)
F_j^{am}	suspended matter flux from atmospheric deposition ($\text{kg m}^{-2} \text{s}^{-1}$)
$F_{s,j}^{am}$	suspended matter radionuclide flux from atmospheric deposition ($\text{Bq m}^{-2} \text{s}^{-1}$)
H_z	thickness of the bottom water layer (m)
Inv_{Cs}	increase in radiocesium derived from FNPP1 until October 31, 2011 (Bq)
K_i	eddy diffusivity ($\text{m}^2 \text{s}^{-1}$)
L	thickness of the seabed sediment active layer (m)
L_b	thickness of the seabed sediment substrate (m)
M_j	suspended matter concentration in size class j (kg m^{-3})
MF_{Cs}	area and time averaged vertical radiocesium flux ($\text{mBq m}^{-2} \text{day}^{-1}$)
Q	river flow flux ($\text{m}^3 \text{s}^{-1}$)
R_j	radius of the suspended matter in size class j (m)
S_d	sources or sinks of dissolved radionuclides ($\text{Bq m}^{-3} \text{s}^{-1}$)
S_j	sources and sinks of suspended matter ($\text{kg m}^{-3} \text{s}^{-1}$)
$S_{s,j}$	sources and sinks of radionuclides in the suspended matter ($\text{Bq m}^{-3} \text{s}^{-1}$)
T	number of days from March 11, 2011 to October 31, 2011 (234 days)
a	constant coefficient
b	constant coefficient

\bar{c}	river mouth cross-sectional averaged sediment concentration (mg l^{-1})
d_{50}	median diameter of the particle size distribution (m)
d_j	diameter of the particles in size class j (m)
$f_{b,j}$	seabed sediment fraction in the substrate (no unit)
f_j	seabed sediment fraction in the active layer (no unit)
$k_{1,j}$	The kinetic coefficient (s^{-1})
$k_{1,j}^m$	kinetic coefficients for adsorption onto the suspended matter (s^{-1})
$k_{1,j}^s$	kinetic coefficient for adsorption onto the seabed sediment (s^{-1})
k_2	kinetic coefficients for desorption from the suspended matter (s^{-1})
p_j	seabed sediment porosity (no unit)
$S_{m,j}$	exchange surfaces for suspended matter in size class j (m^{-1})
$S_{s,j}$	exchange surfaces for seabed sediment particles in size class j (m^{-1})
$w_{s,j}$	settling velocity (m s^{-1})

References

- Ambe, D., Kaeriyama, H., Shigenobu, Y., Fujimoto, K., Ono, T., Sawada, H., Saito, H., Miki, S., Setou, T., Morita, T., Watanabe, T., 2014. A high-resolved spatial distribution of radiocesium in sea sediment derived from Fukushima Dai-ichi Nuclear Power Plant. *J. Environ. Radioact.* 138, 264–275.
- Aoyama, M., Tsumune, D., Uematsu, M., Kondo, F., Hamajima, Y., 2012. Temporal variation of ^{134}Cs and ^{137}Cs activities in surface water at stations along the coastline near the Fukushima Dai-ichi Nuclear Power Plant accident site. *Geochem. J.* 46, 321–325.
- Bezhenar, R., Jung, K., Maderich, V., Willemsen, S., de With, G., Qiao, F., 2016. Transfer of radiocesium from contaminated bottom sediments to marine organisms through benthic food chains in post-Fukushima and post-Chernobyl periods. *Biogeosciences* 13, 3021–3034.
- Blaas, M., Dong, C., Marchesiello, P., McWilliams, J.C., Stolzenbach, K.D., 2007. Sediment-transport modeling on Southern Californian shelves: a ROMS case study. *Contin. Shelf Res.* 27, 832–853.
- Black, E., Buesseler, K., 2014. Spatial variability and the fate of cesium in coastal sediments near Fukushima, Japan. *Biogeosciences* 11, 5123–5137.
- Buesseler, K.O., Jayne, S.R., Fisher, N.S., Rypina, I.I., Baumann, H., Baumann, Z., et al., 2012. Fukushima-derived radionuclides in the ocean and biota off Japan. *Proc. Natl. Acad. Sci. U. S. A.* 109, 5984–5988.
- Buesseler, K.O., Dai, M., Aoyama, M., Benitez-Nelson, C., Charmasson, S., Higley, K., et al., 2017. Fukushima Daiichi-derived radionuclides in the ocean: transport, fate, and impacts. *Ann. Rev. Mar. Sci.* 9, 173–203.
- Choi, Y., Kida, S., Takahashi, K., 2013. The impact of oceanic circulation and phase transfer on the dispersion of radionuclides released from the Fukushima Dai-ichi Nuclear Power Plant. *Biogeosciences* 10, 4911–4925.
- Decho, A.W., Gutierrez, T., 2017. Microbial extracellular Polymeric substances (EPSs) in ocean systems. *Front. Microbiol.* 8, Article 922.
- Fukuda, M., Aono, T., Yamazaki, S., Ishimaru, T., Kanda, J., Nishikawa, J., Otosaka, S., 2018. Factors controlling ^{134}Cs activity concentrations in sediment collected off the coast of Fukushima Prefecture in 2013–2015. *Geochem. J.* 52, 201–209.
- Ikenoue, T., Shimadeta, H., Kondo, A., 2020. Impact of soil erosion potential uncertainties on numerical simulations of the environmental fate of radiocesium in the Abukuma River basin. *J. Environ. Radioact.* 225, 106452.
- Isoguchi, O., Shimada, M., Kawamura, H., 2010. Characteristics of ocean surface winds in the lee of an isolated island observed by synthetic aperture radar. *Mon. Weather Rev.* 139, 1744–1761.
- Iwasaki, T., Nabi, M., Shimizu, Y., Kimura, I., 2015. Computational modeling of ^{137}Cs contaminant trans-fer associated with sediment transport in Abukuma river. *J. Environ. Radioact.* 139, 416–426.
- Jenkins, C.J., 1997. Building offshore soils databases. *Sea Technol.* 38 (12), 25–28.
- Jenkins, C.J., 2002. Automated digital mapping of sediment colour descriptions. *Geo Mar. Lett.* 22 (4), 181–187.
- Kakehi, S., Kaeriyama, H., Ambe, D., Ono, T., Ito, S.I., Shimizu, Y., Watanabe, T., 2016. Radioactive cesium dynamics derived from hydrographic observations in the Abukuma River Estuary, Japan. *J. Environ. Radioact.* 153, 1–9.
- Kamidaira, Y., Uchiyama, Y., Kawamura, H., Kobayashi, T., Furuno, A., 2018. Submesoscale mixing on initial dilution of radionuclides released from the Fukushima Daiichi nuclear power plant. *J. Geophys. Res.: Oceans* 123, 2808–2828.
- Katata, G., Chino, M., Kobayashi, T., Terada, H., Ota, M., Nagai, H., Kajino, M., Draxler, R., Hort, M.C., Malo, A., Torii, T., Sanada, Y., 2015. Detailed source term estimation of the atmospheric release for the Fukushima Daiichi Nuclear Power Station accident by coupling simulations of atmospheric dispersion model with improved deposition scheme and oceanic dispersion model. *Atmos. Chem. Phys.* 15, 1029–1070.
- Kawamura, H., Kobayashi, T., Furuno, A., In, T., Ishikawa, Y., Nakayama, T., Shima, S., Awaji, T., 2011. Preliminary numerical experiments on oceanic dispersion of ^{131}I and ^{137}Cs discharged into the ocean because of the Fukushima Daiichi Nuclear Power Plant disaster. *J. Nucl. Sci. Technol.* 48, 1349–1356.
- Kitamura, A., Yamaguchi, M., Kurikami, H., Yui, M., Onishi, Y., 2014. Predicting sediment and cesium-137 discharge from catchments in eastern Fukushima. *Anthropocene* 5, 22–31.
- Kobayashi, T., Otosaka, S., Togawa, O., Hayashi, K., 2007. Development of a non-conservative radionuclides dispersion model in the ocean and its application to surface cesium-137 dispersion in the Irish Sea. *J. Nucl. Sci. Technol.* 44, 238–247.
- Kusakabe, M., Oikawa, S., Takata, H., Misonoo, J., 2013. Spatiotemporal distributions of Fukushima-derived radionuclides in surface sediments in the waters off Miyagi, Fukushima, and Ibaraki prefectures, Japan. *Biogeosciences* 10, 5019–5030.
- Kusakabe, M., Inatomi, N., Takata, H., Ikenoue, T., 2017. Decline in radiocesium in sea or sediments off Fukushima and nearby prefectures. *J. Oceanogr.* 73, 529–545.
- Le Traon, P.Y., Nadal, F., Ducet, N., 1998. An improved mapping method of multisatellite altimeter data. *J. Atmos. Ocean. Technol.* 15, 522–534.
- Masumoto, Y., Miyazawa, Y., Tsumune, D., Tsubono, T., Kobayashi, T., Kawamura, H., Estournel, C., Marsaleix, P., Lanerolle, L., Avichal Mehra, A., Garraffo, Z.D., 2012. Oceanic dispersion simulations of ^{137}Cs released from the Fukushima Daiichi nuclear power plant. *Elements* 8, 207–212.
- Misumi, K., Tsumune, D., Tsubono, T., Tateda, Y., Aoyama, M., Kobayashi, T., Hirose, K., 2014. Factors controlling the spatiotemporal variation of ^{137}Cs in seabed sediment off the Fukushima coast: implications from numerical simulations. *J. Environ. Radioact.* 136, 218–228.
- Oikawa, S., Takata, H., Watabe, T., Misonoo, J., Kusakabe, M., 2013. Distribution of the Fukushima-derived radionuclides in seawater in the Pacific off the coast of Miyagi, Fukushima, and Ibaraki prefectures, Japan. *Biogeosciences* 10, 5031–5047.
- Otosaka, S., 2017. Processes affecting long-term changes in ^{137}Cs concentration in surface sediments off Fukushima. *J. Oceanogr.* 73, 559–570.
- Otosaka, S., Kato, Y., 2014. Radiocesium derived from the Fukushima Daiichi Nuclear Power Plant accident in seabed sediments: initial deposition and inventories. *Environ. Sci. Process. Impact.* 16, 978–990.
- Otosaka, S., Kobayashi, T., 2013. Sedimentation and remobilization of radiocesium in the coastal area of Ibaraki, 70 km south of the Fukushima dai-ichi nuclear power plant. *Environ. Monit. Assess.* 185, 5419–5433.
- Otosaka, S., Nakanishi, T., Suzuki, T., Satoh, Y., Narita, H., 2014. Vertical and lateral transport of particulate radiocesium off Fukushima. *Environ. Sci. Technol.* 48.
- Periáñez, R., 2008. A modelling study on ^{137}Cs and $^{239,240}\text{Pu}$ behaviour in the Alboran Sea, western Mediterranean. *J. Environ. Radioact.* 99, 694–715, 12.
- Periáñez, R., 2013. Water circulation, sediment transport, and Pollutant dynamics in southern iberia waters: a review on numerical modelling studies. *ISRN Oceanogr.* 27, Article ID 424572.
- Reed, C.W., Niederroda, A.W., Swift, D.J.P., 1999. Modeling sediment entrainment and transport processes limited by bed armoring. *Mar. Geol.* 154, 143–154.
- Roads, J., 2004. Experimental weekly to seasonal U.S. forecasts with the regional spectral model. *Bull. Am. Meteorol. Soc.* 85, 1887–1902.
- Shchepetkin, A.F., McWilliams, J.C., 2005. The regional ocean modeling system (ROMS): a split-explicit, free-surface, topography-following-coordinate oceanic model. *Ocean Model.* 9, 347–404.
- Shchepetkin, A.F., McWilliams, J.C., 2008. Computational kernel algorithms for fine-scale, multiprocess, longtime oceanic simulations. In: Temam, R., Tribbia, J. (Eds.), *Handbook of Numerical Analysis*. Elsevier, Amsterdam, pp. 119–181.
- Sohtome, T., Wada, T., Mizuno, T., Nemoto, Y., Igarashi, S., Nishimune, A., Aono, T., Ito, Y., Kanda, J., Ishimaru, T., 2014. Radiological impact of TEPCO's Fukushima Dai-ichi Nuclear Power Plant accident on invertebrates in the coastal benthic food web. *J. Environ. Radioact.* 138, 106–115.
- Takata, H., Kusakabe, M., Inatomi, N., Ikenoue, T., Hasegawa, K., 2016. The contribution of sources to the sustained elevated inventory of ^{137}Cs in offshore waters east of Japan after the Fukushima dai-ichi nuclear power station accident. *Environ. Sci. Technol.* 50, 6957–6963.
- Takata, H., Kusakabe, M., Inatomi, N., Hasegawa, K., Ikenoue, T., Watanabe, Y., Watabe, T., Suzuki, C., Misonoo, J., Morizono, S., 2017. Long-term distribution of radioactive cesium in the coastal seawater and sediments of Japan. *Rep. Mar. Ecol. Res. Inst.* 22 (Suppl. ment), 17–25.
- Takekawa, K., Nihei, Y., 2013. Correlation between suspended sediment transport and river discharge in Japan. *J. Jpn. Soc. Civil Eng. Ser. B2 (Coast. Eng.)* 69 (No.2), 1, 1221–1225 (in Japanese with English abstract).
- Taniguchi, K., Onda, Y., Smith, H.G., Blake, W., Yoshimura, K., Yamashiki, Y., Takayuki Kuramoto, T., Saito, K., 2019. Transport and redistribution of radiocesium in Fukushima fallout through rivers. *Environ. Sci. Technol.* 53, 12339–12347.
- Tateda, T., Tsumune, D., Tsubono, T., Misumi, K., Yamada, M., Kanda, J., Ishimaru, T., 2016. Status of ^{137}Cs contamination in marine biota along the Pacific coast of eastern

- Japan derived from a dynamic biological model two years. *J. Environ. Radioact.* 151, 495–501.
- Tateda, Y., Misumi, K., Tsumune, D., Aoyama, M., Hamajima, Y., Kanda, J., Ishimara, T., Aono, T., 2020. Reconstruction of radiocesium levels in sediment off Fukushima: simulation analysis of bioavailability using parameters derived from observed ^{137}Cs concentrations. *J. Environ. Radioact.* 214–215, 106172.
- Terada, H., Chino, M., 2008. Development of an atmospheric dispersion model for accidental discharge of radionuclides with the function of simultaneous prediction for multiple domains and its evaluation by application to the Chernobyl nuclear accident. *J. Nucl. Sci. Technol.* 45, 920–931.
- Tsubono, T., Misumi, K., Tsumune, D., Bryan, F.O., Hirose, K., Aoyama, M., 2016. Evaluation of radioactive cesium impact from atmospheric deposition and direct release fluxes into the North Pacific from the Fukushima Daiichi nuclear power plant. *Deep Sea Res., Part I* 115, 10–21.
- Tsumune, D., Tsubono, T., Aoyama, M., Uematsu, M., Misumi, K., Maeda, Y., Yoshida, Y., Hayami, H., 2013. One-year, regional-scale simulation of ^{137}Cs radioactivity in the ocean following the Fukushima Dai-ichi Nuclear Power Plant accident. *Biogeosciences* 10, 5601–5617.
- Tsuruta, T., Harada, H., Misonou, T., Matsuoka, T., Hodotsuka, Y., 2017. Horizontal and vertical distributions of ^{137}Cs in seabed sediments around the river mouth near Fukushima Daiichi Nuclear Power Plant. *J. Oceanogr.* 73, 547–558.
- Uchiyama, Y., Yamanishi, T., Tsumune, D., Miyazawa, Y., 2014b. A regional sediment transport modeling for Fluvial influx and redistribution of suspended radionuclide in the Fukushima coast. *J. Jpn. Soc. Civil Eng. Ser. B2 (Coast. Eng.)* 70 (No.2), 1_571–1_575.
- Usui, N., Wakamatsu, T., Tanaka, Y., Nishikawa, S., Igarashi, H., Nishikawa, H., Ishikawa, Y., Kamachi, M., 2017. Four-dimensional variational ocean reanalysis: a 30-year high-resolution dataset in the western North Pacific (FORA-WNP30). *J. Oceanogr.* 73, 205–233.
- Wang, X.H., 2002. Tide-induced sediment resuspension and the bottom boundary layer in an idealized estuary with a Muddy bed. *J. Phys. Oceanogr.* 32, 3113–3131.
- Wang, C., Baumann, Z., Madigan, D., Fisher, S., 2016. Contaminated marine sediments as a source of cesium radioisotopes for benthic fauna near Fukushima. *Environ. Sci. Technol.* 50, 10448–10455.
- Wilmott, C.J., 1981. On the validation of models. *Phys. Geogr.* 2, 184–194.
- Yamaguchi, M., Kitamura, A., Oda, Y., Onishi, Y., 2014. Predicting the long-term ^{137}Cs distribution in Fukushima after the Fukushima Dai-ichi nuclear power plant accident: a parameter sensitivity analysis. *J. Environ. Radioact.* 135, 135–146.